Journal of Nanobiotechnology

RESEARCH Open Access

M2 macrophage-polarized anti-inflammatory microneedle patch for accelerating biofilm-infected diabetic wound healing via modulating the insulin pathway

Yushan Yang[1†], Limin Fan[1†], Jingsi Jiang[2†], Jiuyuan Sun[1], Liangyi Xue[1], Xiaoyi Ma[1], Le Kuai[3,4], Bin Li[2,4*] and Yongyong Li[1*]

Abstract

Macrophages play a pivotal role in the healing of diabetic ulcers. The sustained elevation of glucose levels damages the insulin signaling pathway in macrophages, leading to dysfunctional macrophages that struggle to transition from pro-inflammatory (M1) to reparative (M2) states. Therefore, modulating macrophage inflammatory responses via the insulin pathway holds promise for diabetic ulcer treatment. Additionally, the presence of biofilm impedes drug penetration, and the resulting immunosuppressive microenvironment exacerbates the persistent infiltration of pro-inflammatory M1 macrophages. Therefore, we designed an array of dissolvable microneedle (denoted as NPF@MN) loaded with self-assembled nanoparticles that could deliver NPF nanoparticles, acid-sensitive NPF-releasing Protocatechualdehyde (PA) with hypoglycemic and insulin-like effects, regulating macrophage polarization to an anti-inflammatory M2 phenotype. Additionally, this study extensively examined the mechanism by which NPF@MN accelerates the healing of diabetic ulcers through the activation of the insulin signaling pathway. Through RNA-seq and GSEA analysis, we identified a reduction in the expression of pathway-related factors such as IR, IRS-1, IRS-2, and SHC. Our work presents an innovative therapeutic approach targeting the insulin pathway in diabetic ulcers and underscores its translational potential for clinical management.

Introduction

Diabetic ulcers (DUs) are a grave complication of diabetes mellitus, frequently characterized by refractory biofilm infections and chronic inflammation [1]. Approximately 25% of individuals with diabetes are affected by DUs, frequently leading to amputation or fatality, with notable financial and social burdens [1, 2]. Hence, there is an urgent devise to explore effective strategies to enhance the healing efficacy of DUs.

The normal process of wound healing is highly coordinated. However, due to the immune imbalance induced by high glucose levels, macrophages face challenges in transitioning from an inflammatory phenotype (M1) to

†Yushan Yang, Limin Fan and Jingsi Jiang contributed equally to this work.

*Correspondence:
Bin Li
lib@shskin.com
Yongyong Li
yongyong_li@tongji.edu.cn

Full list of author information is available at the end of the article

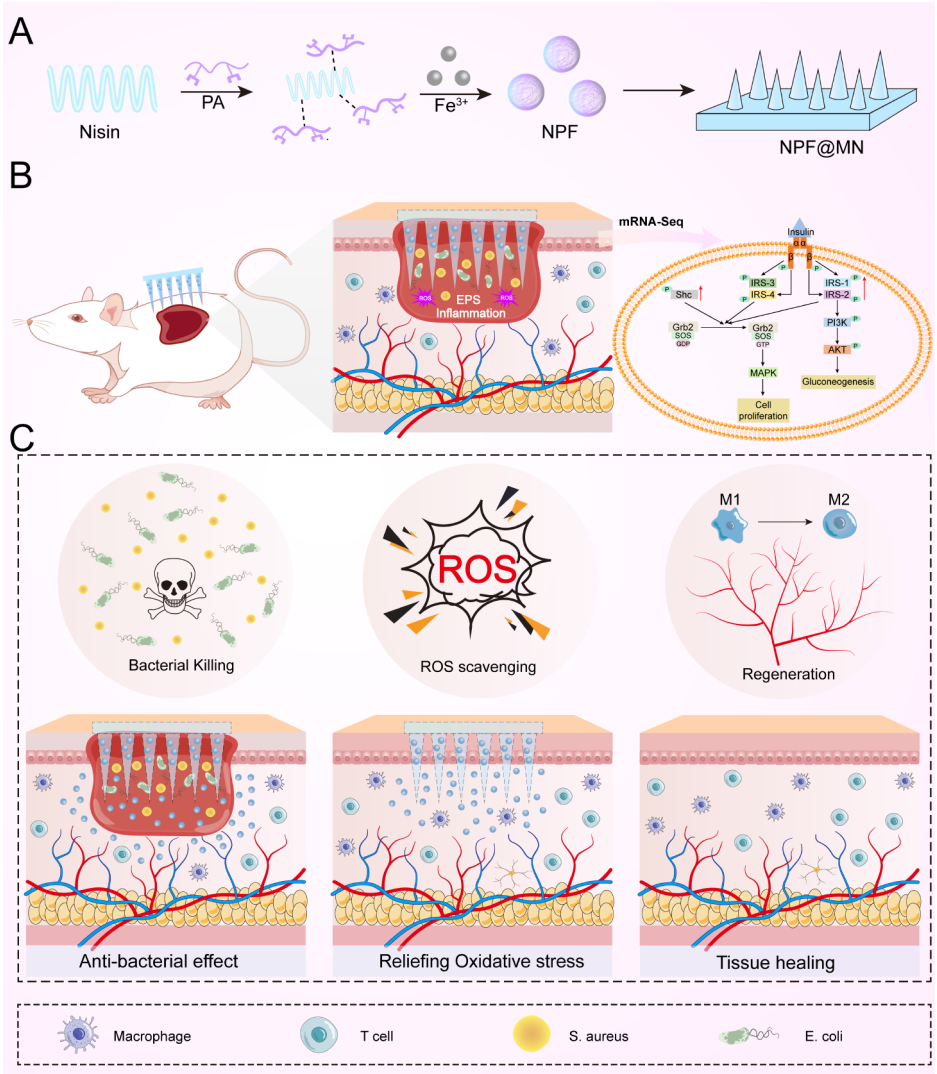

Keywords Microneedle, Biofilm, Macrophage, Insulin pathway, Diabetic ulcers healing

a reparative phenotype (M2) [3]. This results in diabetic ulcers remaining in a state of chronic inflammation and difficulty in entering the tissue repair phase [4, 5]. The continuous accumulation of M1 macrophages and the secretion of pro-inflammatory cytokines or chemokines further recruit monocytes to infiltrate and differentiate into the M1 phenotype, leading to oxidative stress at the wound site [6, 7]. This further increases the risk of biofilm infection and hinders the transition of wounds from the inflammatory to proliferative phases [8, 9]. Thus, the immune microenvironment of DUs can be modulated by mediating the M2 phenotypic polarization of macrophages to restore dysregulated immune processes.

Persistent hyperglycemia-induced damage to the insulin signaling pathway in diabetic ulcers leads to delayed wound healing [10–12]. High glucose exposure has been shown to induce macrophage polarization toward the M1 phenotype, which can be reversed by insulin stimulation [13–15]. Further studies on the cellular and molecular mechanisms of insulin-induced inflammation regression have revealed that insulin can enhance the transformation of macrophages into the M2 phenotype via PI3K/Akt and PPAR-γ signaling pathways [16]. However, prolonged local insulin injections can lead to significant side effects, and insulin resistance can exacerbate biofilm formation [17]. Polyphenolic compounds have gained attention due to their high bioavailability and anti-hyperglycemic effects with fewer side effects [18, 19]. Protocatechualdehyde (PA), extracted from Chinese herbal Salvia root, is an approved drug known for its anti-inflammatory properties, antibacterial and possible hypoglycemic effects [18, 20–22]. In contrast to natural polyphenolic

compounds such as catechins and epigallocatechin gallates, PA has an aldehyde group that can form reversible Schiff base bonds with amino groups [23]. The study found that phenolic active compounds like Protocatechualdehyde displayed strong interactions with four receptor proteins, namely IRS1, PI3K, Akt, and GLUT4, within the insulin signaling pathway [24]. Network pharmacology and mechanism validation showed that a variety of phenolic substances could improve insulin resistance via IRS-1/PI3K/Akt pathway [24–26]. Thus, PA may facilitate wound healing by activating the insulin pathway and promoting macrophage M2 polarization.

However, the dense structure of biofilm limits drug permeability, resulting in reduced efficacy and potential drug resistance [27–29]. Furthermore, bacterial infection exacerbates inflammation at the wound site, increasing the macrophage M1/M2 ratio [8, 30]. Antimicrobial peptides (AMPs), such as Nisin, have been widely used to clear biofilms [31–33]. However, uncontrolled antimicrobial function during storage, susceptibility to environmental stresses, and sensitivity to proteolysis are the most common challenges to Nisin, hindering its potential therapeutic applications [10]. In order to achieve simultaneous integration of macrophage polarization and bactericidal capabilities, self-assembled nanomaterials have become a very attractive and valuable topic for the treatment of DUs with biofilm infections. Notably, microneedle (MN) patches have emerged as a novel approach, which has recently been reported for the treatment of bacterial biofilms [34–36]. The utilization of MN containing antimicrobial agents has been shown to be an effective method for the treatment of chronic wound biofilms.

Based on the above considerations, beginning with the regulation of the insulin pathway to promote macrophage M2 polarization and improve the efficiency of biofilm clearance, thereby modulating the immune microenvironment, we have developed a multifunctional dissolving microneedle based on acid-responsive Nisin@PA@Fe (NPF) nanoparticles of the antimicrobial peptide Nisin [31, 37], thereby accelerating wound healing in biofilm infection. Briefly, the hydroxyl-aldehyde addition reaction between the hydroxyl group in Nisin and the aldehyde group in PA forms a catechol ion coordination bond with metal ions (Fe^{3+}) [38, 39]. This process leads to a distinctive chemical cross-linking self-assembly resulting in the formation of NPF, which is then loaded onto hyaluronic acid microneedle patches. NPF@MN exhibited properties of anti-biofilm, anti-inflammatory, pro-M2 polarization and accelerated tissue repair. In order to explore the mechanism of NPF@MN in the conquest of depleted uranium biofilms and chronic healing, RNA-seq and GSEA analysis were performed in this study, and the insulin signaling pathway was identified as a key regulatory pathway. The findings suggest that NPF@MN can reduce persistent chronic inflammation and promote chronic wound healing by activating the insulin signaling pathway. The study offers novel insights into designing all-in-one therapies with immunomodulatory capabilities and holds significant clinical translational potential.

Results

Synthesis and characterization of NPF

It has been reported that natural protocatechualdehyde, such as PA, can combine with primary amines to form reversible Schiff base bonds [40]. The polyphenol structure also easily coordinates with trivalent iron ions at pH greater than 8.5 [41, 42], which drives self-assembly into stable nano agglomerates [42]. Additionally, the introduction of coordination bonds not only accelerates nano-self-assembly but also coordinates with Fe^{3+} to protect PA from autooxidation at high pH [43, 44]. Due to the pH-dependent Schiff base bond and the coordination of Fe^{3+} and PA, the nanoparticles can be released in acidic environment. Based on this, we have prepared nanoparticles NPF.

The Preparation of NPF involved the reaction of ferric chloride hexahydrate ($FeCl_3{\cdot}6H_2O$) with PA in an aqueous solution of Nisin at room temperature. As shown in Fig. 1A. To ensure that antioxidant activity dominates, we explored the suitable molar ratio of PA/Fe, and finally designed the molar ratio of PA/Fe to be 3:1 (Figure S1, S2), much higher than their pro-oxidative concentration (PA: Fe;1:1) [45, 46], which was consistent with the literature [46, 47]. To confirm the successful synthesis of Schiff base bonds, the chemical structure of Nisin-PA was analyzed using Fourier transform infrared spectrum (FTIR), ^1H NMR spectroscopy, and ultraviolet absorption spectroscopy (UV-Vis). The -C=N- tensile vibration peak by FTIR (Fig. 1B) at 1622 cm^{-1} confirmed the formation of Schiff base bonds between amino groups in Nisin and the aldehyde groups in PA. At the same time, ^1H NMR spectrum also confirmed the successful synthesis of Nisin-PA (Figure S3). Additionally, the UV-Vis absorption spectrum of Nisin-PA was significantly different from that of Nisin and PA (Fig. 1C), and the characteristic absorption peak of Nisin-PA at 256 nm was located at the position of benzene ring $\pi \rightarrow \pi^*$, which further confirmed the successful synthesis of Nisin-PA. Based on the Nisin-PA structure, self-assembly into NPF was then driven by polyphenol ferro-phenol complexation. After complexing iron ions, Nisin-PA complexes exhibited a typical ligand-metal charge transfer characteristics band. The UV spectrum showed that NPF had a broad absorption band at 500–650 nm, confirming the coordination of Fe^{3+} with PA [47] (Figure S4).

The hydrodynamic diameter of NPF determined by dynamic light scattering (DLS) was 60 nm with a narrow

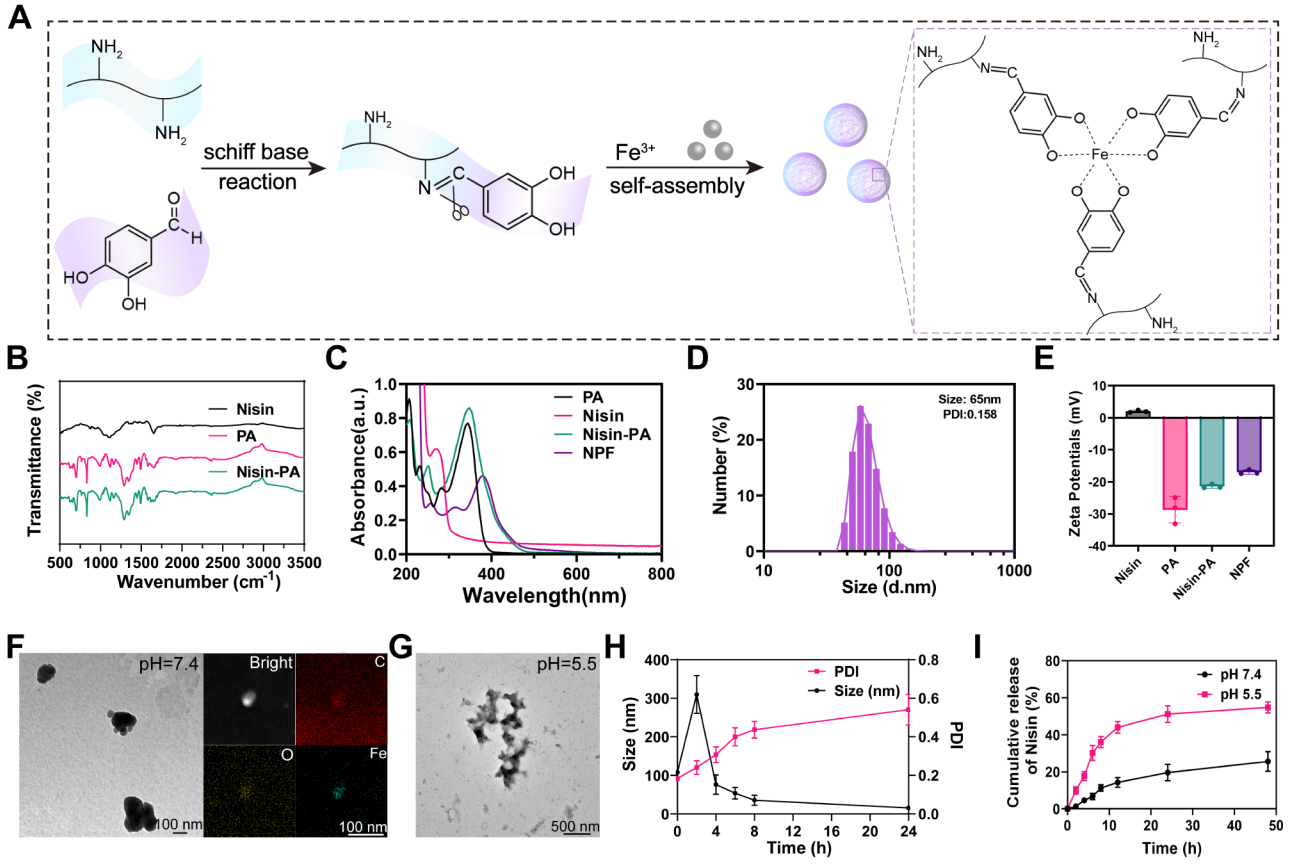

Fig. 1 Synthesis and characterization of NPF. (**A**) Schematic illustration of the synthetic process of NPF. (**B**) FTIR spectra and (**C**) UV-vis absorption spectra of Nisin, PA, and Nisin-PA. (**D**) DLS of NPF at pH 7.4. (**E**) Zeta-potential of Nisin, PA, Nisin-PA, NPF. (**F**) TEM image and SEM image of elemental mapping of NPF at pH 7.4 and (**G**) TEM image of NPF at pH 5.5. (**H**) Size and PDI variations of NPF at pH 5.5 buffers. (**I**) In vitro release profiles of Nisin in different pH buffers (pH 5.5 and pH 7.4). Data are shown as the mean ± SD ($n = 3$)

size distribution (PDI = 0.158) (Fig. 1D), and the zeta potential was negative (Fig. 1E). Notably, the zeta potential of NPF changed from positive to negative following the addition of PA and Fe^{3+}(Fig. 1E), which may be due to the abundance of phenolic hydroxyl groups in PA. Additionally, the stability of NPF in PBS and PBS containing 5% FBS was studied by monitoring the changes in particle size over time and the results showed that the size of NPF remained stable within 24 h (Figure S5), Homogeneous spherical NPF of uniform size were observed through transmission electron microscopy (TEM) imaging (Fig. 1F), consistent with the DLS results. The composition of the NPF was confirmed by bright-field scanning electron microscopy (Fig. 1F), showing a uniform distribution of carbon (C), iron (Fe), and oxygen (O) in NPF. The iron content was quantified using inductively coupled plasma-optical emission spectrometry (ICP-OES) and determined to be 15.76 ± 0.86w/w (Figure S6).

In order to evaluate the pH-responsive behavior of nanoparticles, the morphology of NPF was studied at pH 5.5. It was observed that NPF exhibited pH-dependent disassembly behavior (Fig. 1G), and the circular particle morphology became irregular and blurred. Moreover, as shown in Fig. 1H, the size distribution and PDI of NPF were relatively stable at pH 7.4, but gradually increased and aggregated and then dissociated at pH 5.5, which was consistent with the phenomenon observed in TEM images. Moreover, the zeta potential rebounded from −18.3 mv to 2.36 mv under acidic conditions (pH 5.5) (Figure S7). All of these indicated the presence of dynamic cleavage of acid-sensitive Schiff base bonds in NPF. Due to the pH dissociation of the nanostructure, NPF exhibited pH-dependent release behavior. The release of Nisin at pH 7.4 and pH 5.5 was quantified according to the UV standard curve (Figure S8), and the cumulative released rates of buffer for 48 h were 25.64%±5.29, 54.81%±3.05, respectively (Fig. 1I).

Synthesis and characterization of NPF@MN

To disrupt biofilms and increase drug permeability, NPF were further loaded into MN. In a typical experiment, NPF@MN were prepared using micromolding techniques (Fig. 2A). Specifically, low molecular weight HA powder was first dissolved with an aqueous solution of

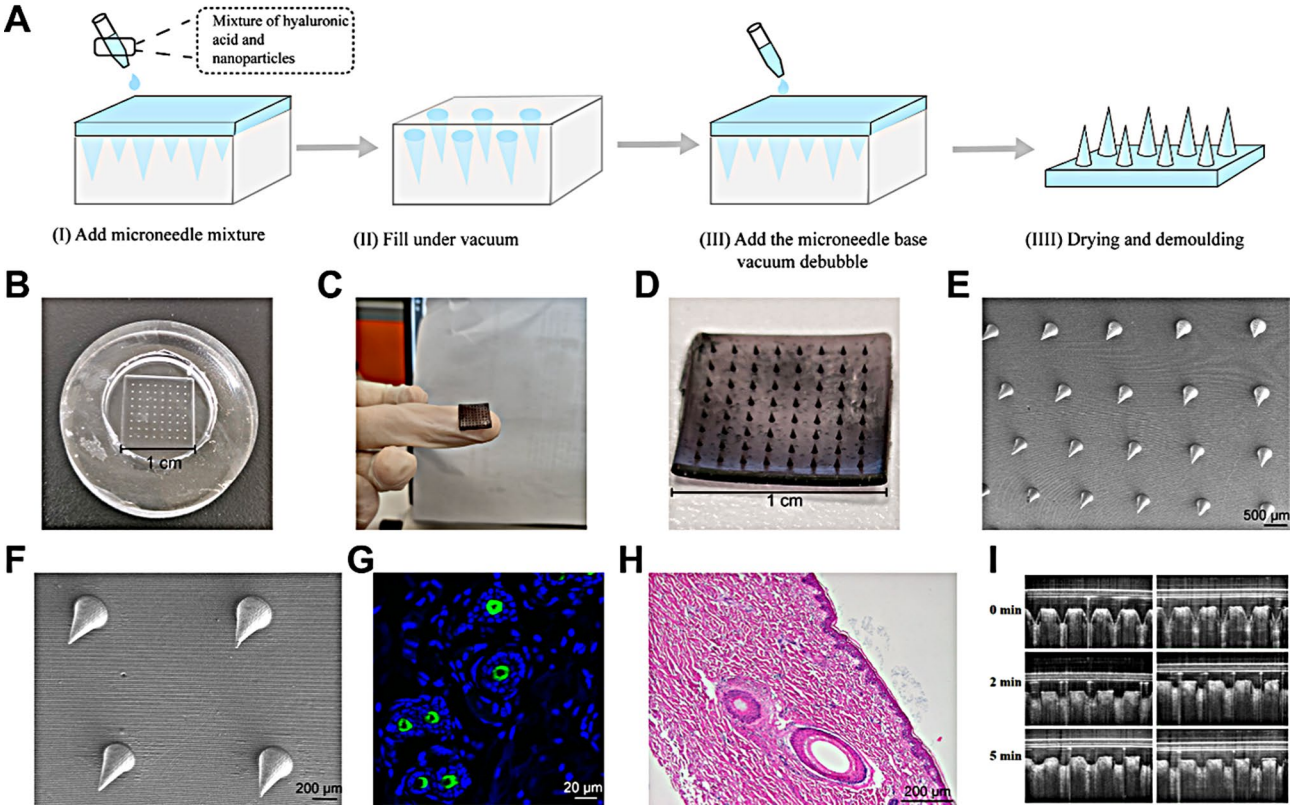

Fig. 2 Synthesis and characterization of NPF@MN. (**A**) Synthesis schematic of NPF@MN. (**B**) Image of PDMS MN mold. (**C**, **D**) Top-down and isometric views of an NPF@MN, as shown in photographic images. (**E**, **F**) SEM images of NPF@MN. Bar = 500 μm and 200 μm, respectively. (**G**) Green fluorescence signal of FITC in a cross-section of the skin of a small fragrant pig. Bar = 20 μm. (**H**) Histological section depicting the microneedle aspiration site. Bar = 200 μm. (**I**) Brightfield morphological images of NPF@MN at various time points post-moisture absorption (in a 75% humidity environment at room temperature)

NPF, loaded into the MNs tip and substrate and then the NPF@MN were prepared under vacuum using a PDMS (polydimethylsiloxane) (Fig. 2B) mold. As shown in Fig. 2C, D, the resulting microneedle patch was arranged in an 8×8 MN array, and the tip of the NPF@MN was dark translucent due to the addition of NPF. We then performed the morphological characterization by using brightfield scanning electron microscopy (SEM) and Optical Coherence Tomography (OCT) (Fig. 2E-F, Figure S9). The successful NPF@MN was prepared into a conical needle-like structure with uniform distribution, tip diameter of 250 μm, height of 600 μm and needle spacing of 500 μm. Of note, the thickness of the biofilm of 10–100 μm [48] is much smaller than the length of the microneedle tip, and since most of the microvascular in the dermis layer of the skin is located 1–2 mm below the epidermis [49], the microneedle tip could penetrate the biofilm and avoid contact with nerve fibers and capillaries.

In order to observe the permeability of the drug in the skin, soluble microneedle patches based on fluorescein isothiocyanate (FITC) were prepared. These patches were inserted into the skin of small fragrant pig. Figure 2G showed that MN could puncture the epidermis and promote FITC dye diffusion, indicating that the drug could rapidly diffuse into the skin with the insertion of MNs. The fluorescent dye rhodamine B (RhB) was used as a model drug for visual analysis. The drug-loaded microneedle (RhB@MN) demonstrated higher penetration and drug delivery efficiency compared to free RhB on isolated skin (Figure S10). Therefore, NPF@ MN offer a simple and efficient approach to drug delivery. Subsequently, we further investigated the insertion ability of NPF@MN on healthy skin in mice. The mechanical properties of the NPF@MN were measured by force-displacement curves, and NPF@MN did not show any breaking points and had a mechanical force (>0.098 N) that penetrated the skin (Figure S11). Hematoxylin and eosin (H&E) (Fig. 2H) showed successful penetration of the normal epidermis by the microneedle patches. In addition, microneedles penetrating the skin could also be observed through OCT, causing microscopic damage and tiny channels (Figure S12).

To assess the biodegradability of NPF@MN, its hygroscopicity was evaluated. The NPF@MN was placed in an airtight container with a specific humidity and the

morphological changes of the NPF@MN are recorded in real time (Fig. 2I). After 5 min in the humidity chamber, a noticeable solubilization state of the MN tips was observed. The remarkable hygroscopicity of MNs could absorb excessive tissue penetrating fluid produced by the wound, providing a good environment for wound healing. Furthermore, the NPF@MN completely dissolved within 20 min after immersion in an aqueous solution, and the drug contained within it was released quickly. Therefore, only drug-loaded nanoparticles were measured for drug release spectra, but not arrays containing drug-loaded microneedles.

In vitro antioxidant capabilities and anti-inflammatory of NPF@MN

PA is a naturally occurring phenolic that exhibits good biocompatibility and free radical scavenging energy, which can protect cells from oxidative damage and accelerate wound healing [41]. Fe^{3+} was introduced into the physical complexation of catechol groups to reduce the oxidation of PA. Based on this, we tested the ROS scavenging capacity of NPF (Fig. 3A). The oxidation resistance of the sample was first determined by an experiment to scavenge the stable free radical 1,1-diphenyl-2-picrylicyl (DPPH). As shown in Fig. 3B, the inhibition rate of DPPH radicals was proportional to the NPF concentration nanoparticles. When the concentration of NPF was higher than 125 μg/mL, the inhibition rate was higher than 80%, indicating that NPF could effectively remove DPPH. We employed the standard antioxidant vitamin C as a control to evaluate the antioxidant capacity of NPF. As shown in Fig. 3C, the antioxidant capacity of NPF is comparable to that of vitamin C. The characteristic absorption peak of DPPH at 517 nm was monitored using UV light. Both NPF and vitamin C exhibited peaks that were slightly lower than that of the control group, which showed almost no absorption peak at 517 nm (Fig. 3D). Subsequently, we separately analyzed hydroxyl radicals (·OH) and superoxide anions ($O_2^{\bullet-}$), the main ROS species of diabetic wounds. The fluorescence signal at 425 nm in Figure S13 diminishes progressively with increasing concentrations of NPF, demonstrating that NPF effectively scavenges hydroxyl radicals in a concentration-dependent manner. Quantitative analysis of hydroxyl radical scavenging (Figure S14) indicated that at an NPF concentration of 250 μg/mL, approximately 50% of the hydroxyl radicals were scavenged. To assess the superoxide anion scavenging capacity, we measured the inhibition ratio of the photoreduction of nitroblue tetrazolium (NBT). The characteristic signal of the radical at 560 nm weakened with increasing NPF concentration (Fig. 3E), indicating a concentration-dependent superoxide anion scavenging. At an NPF concentration of 250 μg/mL, over 90% of $O_2^{\bullet-}$ in solution was scavenged. Figure 3F shows the low peaks of NPF and vitamin C at 560 nm, with similar peaks for NPF and vitamin C, and quantitatively confirms that NPF and vitamin C have comparable O_2•- clearance capacity (Figure S15). These findings collectively indicate that NPF exhibits a potent capacity to scavenge ROS and protect cells from oxidative damage.

Before studying the ability of NPF to clear hydrogen peroxide-induced intracellular ROS, we first evaluated the biocompatibility of the material, which is an important prerequisite for further biomedical applications. The hemolytic test (Figure S16) was initially employed to evaluate the biocompatibility of the materials. Subsequently, 293T cells were selected to assess their viability following different treatments. The viability of cells decreased gradually with increasing concentration of each treatment group, and when the NPF concentration was 300 μg/mL, the cell survival rate exceeded 90% (Figure S17). Furthermore, the live/dead staining results depicted in Figure S18 revealed that 300 μg/mL NPF did not induce significant cell death after 24 h of incubation with cells relative to the control group. Cell proliferation was accelerated by NPF, NPF@MN and r-bFGF treatments instead of blank MN (Fig. 3G) in human immortal keratinocyte line (HaCaT). Subsequently, the ability of NPF nanoparticles to scavenge ROS was evaluated in the presence of human dermal fibroblasts 3T3. As shown in Fig. 3H, human dermal fibroblasts were incubated with 3 mmol of H_2O_2, resulting in distinct green fluorescence. In contrast, fluorescence intensity was significantly reduced when cells stimulated with the same amount of H_2O_2 were treated with 150 μg/mL of NPF. With the increase in NPF concentration, the fluorescence was further weakened. In addition, NPF@MN was soaked in DMEM medium for 30 min to obtain an extract of approximately 310.4 μg/mL NPF for cell radical scavenging experiments. When cells were cultured in medium containing NPF@MN extract (approximately 310.4 μg/mL), ROS concentration also decreased significantly, and quantification showed fluorescence intensity comparable to NPF at a concentration of 300 μg/mL (Fig. 3I).

Macrophages, a crucial component of the innate immune system, exhibit diverse M1/M2 phenotypic levels that significantly influence the wound healing process. The overproduction of reactive oxygen species (ROS) in diabetic ulcers disrupts inflammatory regulation, leading to an imbalance in macrophage phenotypes [50]. Our study aimed to ameliorate the inflammatory microenvironment using NPF@MN, thereby promoting the shift of macrophages from the classically activated M1 phenotype to the alternatively activated M2 phenotype. Flow cytometry analysis further corroborated these findings, showing that LPS-treated RAW264.7 cells had an increased proportion of CD206-positive cells and

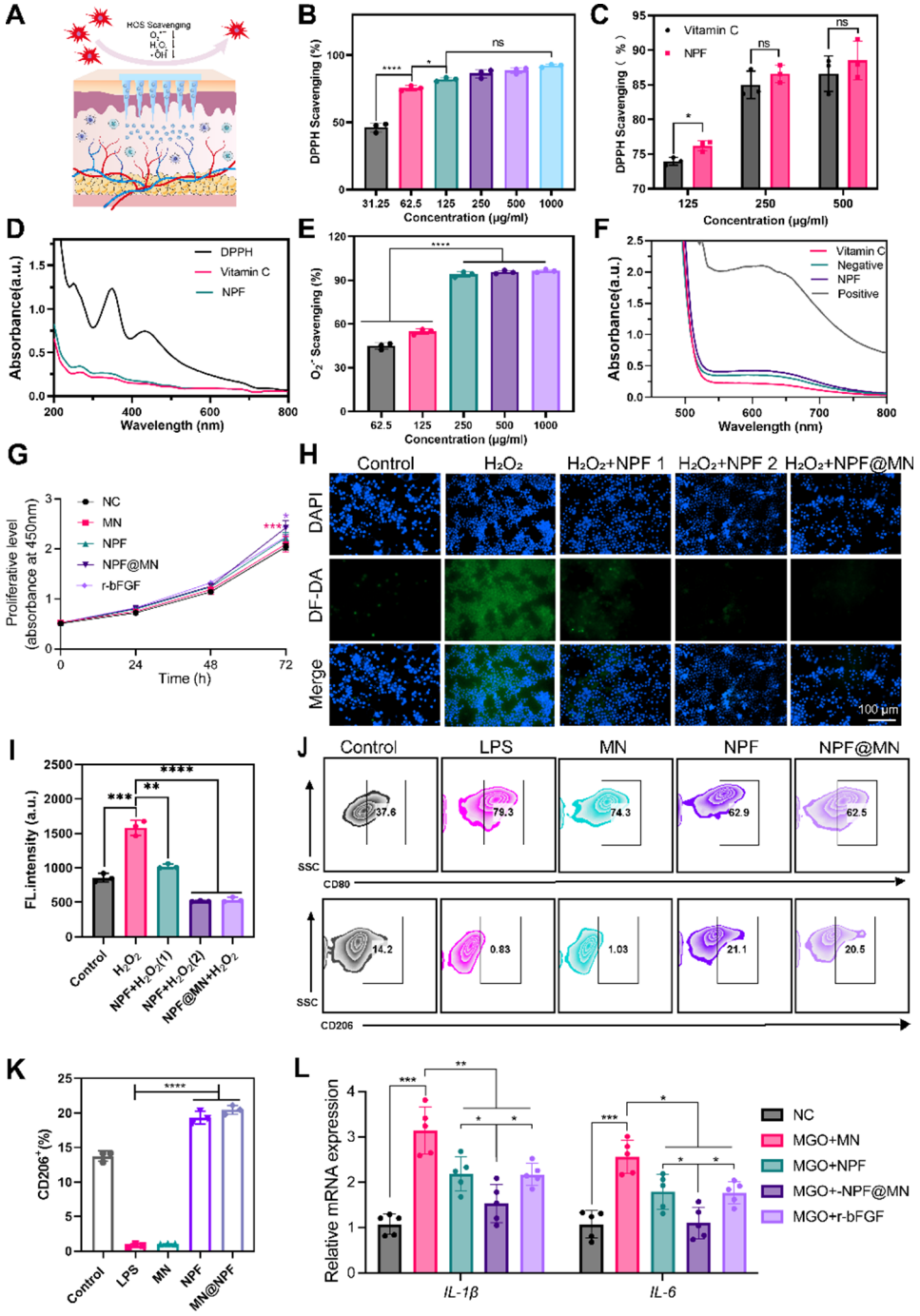

Fig. 3 In vitro antioxidant capabilities of NPF@MN. (**A**) Schematic diagram of DPPH oxidation resistance. (**B**) Antioxidant activity of NPF measured with the (DPPH) radical scavenging activity assay. $n = 3$ samples/group. (**C**) DPPH clearance of different concentrations of vitamin C and NPF ($n = 3$ samples/group) and (**D**) DPPH assay absorbance curves. (**E**) Quantitative plot of NPF scavenging capacity for $O_2^{\bullet-}$ and (**F**) Complete scan curves of NPF and vitamin C in the $O_2^{\bullet-}$ clearance assay. (**G**) The proliferation levels of HaCaT cells with different interventions (50 μg/mL of NPF/NPF@MN). $n = 3$ samples/group. (**H**) Fluorescence images of ROS in different groups of 3T3 cells treated with DCFH-DA. 150 μg/mL for NPF 1 and 300 μg/mL for NPF 2, Scale bar = 100 μm. (**I**) Quantification of the DCFH-DA dye fluorescence intensity extracted from (**H**) (**J**) CD80/CD206 flow cytometry of RAW264.7 cells treated with LPS, LPS + MN, or LPS + NPF@MN for 24 h (**K**) Quantification of the $CD206^+$of RAW264.7 cells intensity extracted from (**J**). (**L**) The mRNA expressions of inflammatory cytokines *IL-1β* and *IL-6* determined by qPCR. $n = 5$ samples/group. $^{****}P < 0.0001$, $^{***}P < 0.001$, $^{**}P < 0.01$, $^{*}P < 0.05$, ns represented not significant

a decreased proportion of CD80-positive cells following incubation with NPF@MN (Fig. 3J, K, Figure S19). Western blot analysis (Figure S20) quantified the CD80 and CD206 protein levels, revealing trends consistent with the immunofluorescence staining and flow cytometry data. Additionally, we analyzed the expression levels of the pro-inflammatory cytokine *IL-1β* and the anti-inflammatory cytokine *IL-10* (Figure S21). The results demonstrated that NPF@MN treatment upregulated *IL-10* and downregulated IL-1β, indicating a reduction in M1 expression and an increase in M2 expression. In vitro inflammatory model of DU by methylglyoxal (MGO), the mRNA expression levels of *IL-1β* and *IL-6* were upregulated significantly, while reductions were observed in MN, NPF@MN and rb-bFGF groups (Fig. 3L). Among them, NPF@MN showed the most obvious effect. In summary, these findings suggest that NPF@MN can effectively induce macrophage polarization towards the M2 phenotype, thereby exerting significant immunomodulatory effects.

In vitro antibacterial capabilities of NPF@MN

Biofilm is another barrier that hinders the closure of diabetic ulcers and further impede wound healing [51]. Therefore, it is essential to eliminate biofilms on the wound surface and improve the quality of life for patients.

To evaluate the bacteriostatic activity of acid-responsive NPF, disc diffusion assays were employed to test the antimicrobial properties of MNs and NPF@MN against *S. aureus*. The NPF@MN were cultured with *S. aureus* at 37 °C for 24 h. As shown in Fig. 4A, a significant inhibition zone was observed only around the NPF@MN at pH 5.5, but no obvious inhibitory zone was observed around the blank microneedle or the control group, indicating that NPF had a significant inhibitory effect on the growth of *S. aureus* under acidic conditions at pH 5.5. Conversely, the blank MN did not exhibit any antibacterial effect, while the NPF@MN in the neutral environment had a weak antibacterial effect, which may be due to the degradation of nanoparticles over time, resulting in the slow release of the drug and thus playing a weak antibacterial effect. As shown in Fig. 4B, NPF@MN rapidly killed *S. aureus* in acidic liquid cultures. All bacteria in the culture were killed within 12 h, and none of the control groups significantly affected the bacterial count of *S. aureus*.

In addition, the plate counting method (SPM) was used to study the antibacterial effect of acid-responsive nanoparticles on *S. aureus* and *E. coli*. Figure 4C quantitatively showed the antibacterial effect of different concentrations of NPF on *S. aureus* and *E. coli*, with colonies in the 800 μg/mL group being basically absent, indicating a significant reduction in the viability of *S. aureus and E. coli*. Counting analysis of bacterial colonies revealed that the antibacterial effect of NPF treatment was significant as the NPF concentration increased from 100 μg/mL to 800 μg/mL, compared to the control group, and the antibacterial rate was 99.6% when the NPF concentration was 800 μg/mL (Fig. 4D, E).

MNs with or without NPF nanoparticles were incubated with two bacterial strains (*S. aureus* and *E. coli*) at different pH conditions, and then stained by Live/Dead bacteria. The results for *E. coli* and *S. aureus* were consistent, with the bacterial effectively killed when incubated on discs with NPF and in an acidic environment. As shown in Fig. 4F, the surface of blank MNs incubated with bacteria under neutral conditions displayed strong green fluorescence due to bacterial adhesion and proliferation, while the surface coated with NPF under acidic conditions showed stronger red fluorescence, indicating effective bacterial killing. Furthermore, under neutral conditions, the red fluorescence incubated by NPF was slightly stronger than that of the blank MNs set, which may be due to the sustained release of the nanoparticles exerting certain antibacterial activity, and also indicates that NPF was acid-responsive and had a higher release rate under acidic conditions. Consistent trends were also obtained by ImageJ analysis of the red fluorescence intensity in each group (Figure S22).

In vitro anti-biofilm activity

It is generally believed that most bacteria can form biofilms on the surface of chronic wounds, and this barrier of dense extracellular polymers can resist the penetration of antimicrobials. Hence, exploring the anti-biofilm efficacy of NPF@MN is imperative. Crystal violet staining was employed to assess the spread of biofilms created by E. coli and S. aureus across varying pH levels. As shown in Fig. 5A and B, NPF@MN had almost no dispersion effect on biofilms at pH 7.4. However, at pH 5.5, after incubation with bacteria, crystal violet diffused containing NPF@MN, and only a small amount of crystal violet was observed. Compared with the crystalline violet diffusion effect of *S. aureus*, *E. coli* was relatively weak, indicating that the antibacterial effect of micro-drug loading on Staphylococcus aureus was better. This may be due to Nisin's better antimicrobial selectivity against gram-positive bacteria than gram-negative bacteria [52]. The biofilm biomass was shown in Fig. 5B was consistent with Fig. 5A. As shown in Fig. 5C. Compared to blank microneedle patches, both NPF@MN-treated *S. aureus* and *E. coli* biofilms showed strong red fluorescence, only weak green fluorescence, and a significant reduction in total bacterial count at pH 5.5. Image J was further used to quantify the fluorescence intensity of biofilms (Fig. 5D and E). The results showed that NPF@MN produced red fluorescence intensity that was higher than the blank MNs control group when incubated with biofilms of *S.*

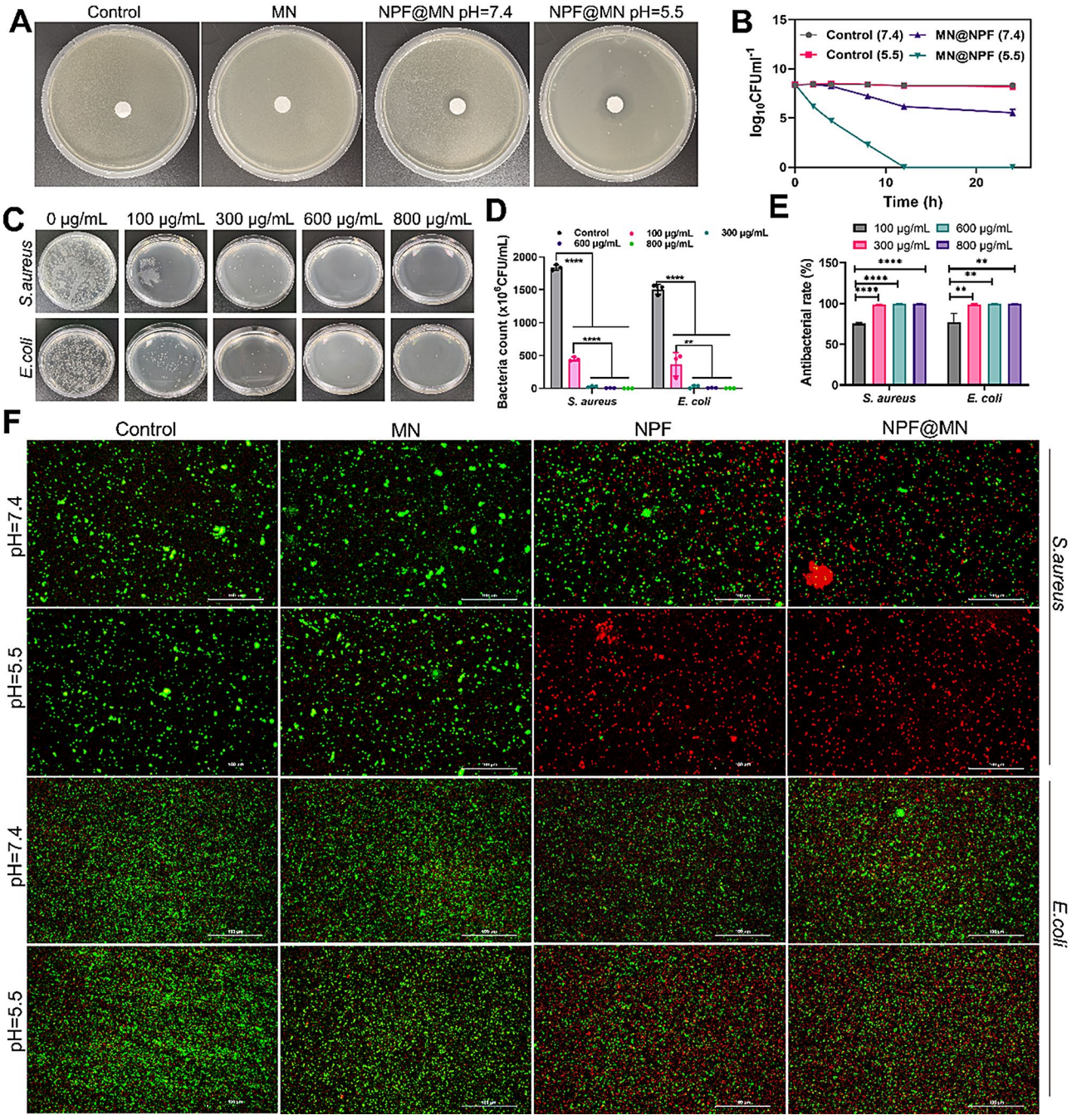

Fig. 4 In vitro antibacterial capabilities of NPF@MN. (**A**) Representative photographic images of *S. aureus* treated with MN patches in different pH. (**B**) Log10 CFU/mL of *S. aureus* monitored when exposed to PBS (control), NPF@MN (pH = 7.4), and NPF@MN (pH = 5.5) for 24 h; The antibacterial activity of NPF@MN against ***E****. coli* and *S. aureus* determined through (**C**-**E**) CFU assays and (**F**) live/dead staining recorded after incubation for 2 h. Scale bar = 100 μm $n = 3$ samples/group. $^{****}P < 0.0001$, $^{***}P < 0.001$, $^{**}P < 0.01$

aureus and *E. coli* at pH 5.5, respectively. This was due to the positive antibacterial effect of NPF.

In addition, to better understand the behavior of the NPF@MN in the intended application, we performed in vitro antimicrobial test on ex vivo pig skin using *S. aureus*. As shown in Fig. 5F, the biofilm of *S. aureus* formed by the control group and the blank microneedle patches control group after incubation with ex vivo pig skin was more obvious than that produced by the NPF@MN experimental group. However, when using MNs containing NPF, there was visible evidence of the degradation of NPF@MN patches and NPF released to the wound site, as shown in Fig. 5G, biofilms treated with NPF@MN showed a reduction of *S. aureus*. Additionally,

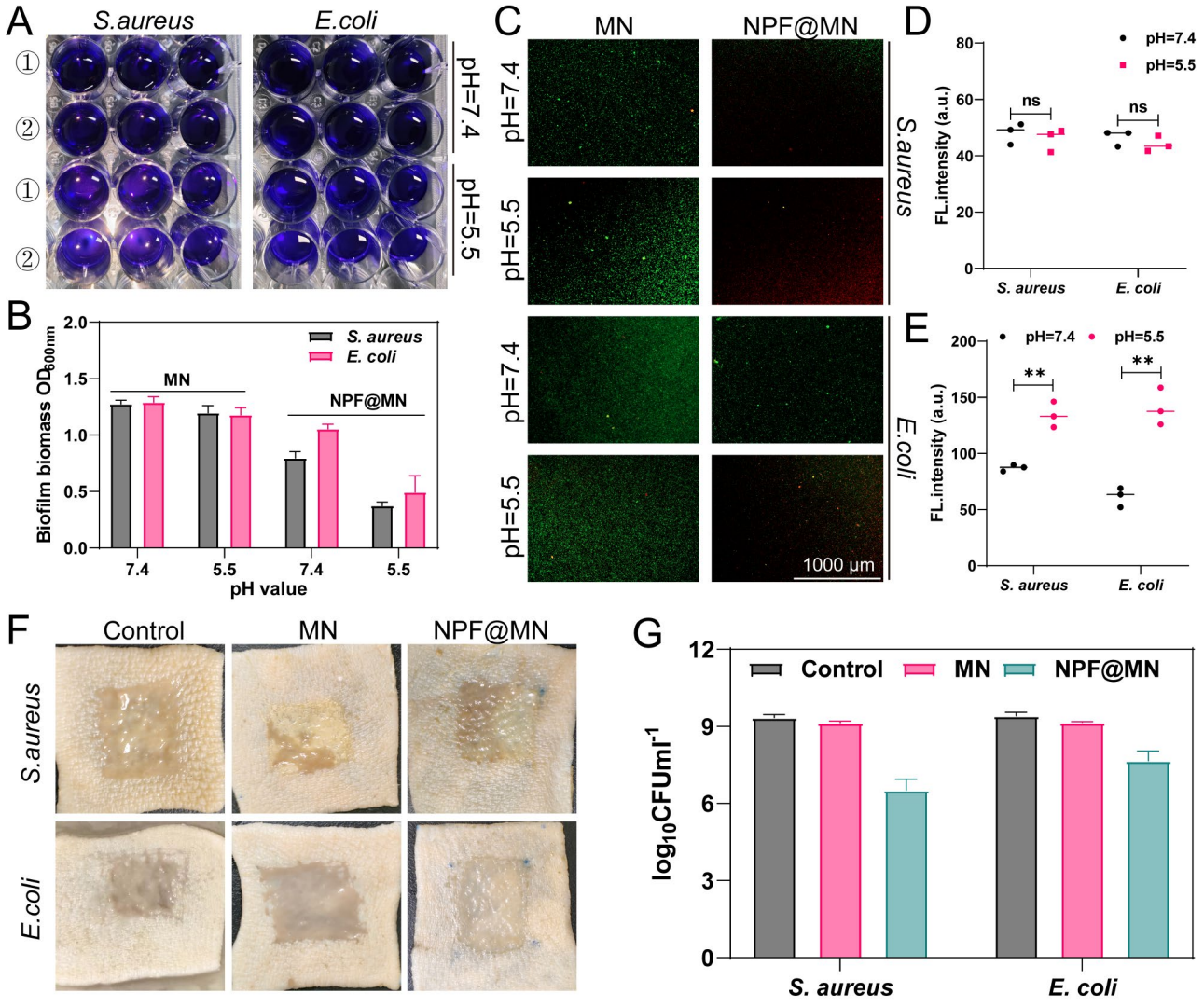

Fig. 5 In vitro anti-biofilm activity. Images depicting crystal-violet-stained biofilms of (**A**) S. aureus and E. coli following incubation with MN (①) and NPF@MN (②) under pH 7.4 and pH 5.5 conditions. Additionally, (**B**) illustrates the biofilm biomass of E. coli and S. aureus treated with MN and NPF@MN under pH 7.4 and pH 5.5, respectively. (**C**) Further analysis was conducted using confocal laser scanning microscopy (CLSM) of biofilms of E. coli and S. aureus post-incubation with MN and NPF@MN under pH 7.4 and pH 5.5 for 2 days, with a scale bar set at 1000 μm. The fluorescence intensity of red-stained biofilm (indicative of dead bacteria) following treatment with (**D**) MN and (**E**) NPF@MN was quantified using Image J. Viable bacterial cells exhibiting intact cell membranes emit green fluorescence, while dead bacterial cells with damaged membranes predominantly fluoresce red. (**F**) In vitro *E. coli* and *S. aureus* assays on a porcine skin infection wound model. (**G**) Log_{10} CFU/mL of Control group, MNs, and with NPF@MN. $^{**}P < 0.01$, ns represented not significant

because MNs are convenient and painless, the patch can simply be applied multiple times to completely eradicate biofilms in potential clinical practice.

NPF@MN rescued S. aureus-infected diabetic wounds

To further testify the efficacy of NPF@MN in treating diabetic ulcers (DUs) against *S. aureus* biofilms, we established *S. aureus* biofilms in STZ-induced diabetic mouse wounds and treated with different interventions (Fig. 6A). The concentration of 300 μg/mL was applied to the following experiments since it showed the most efficient effect (Figure S23). In order to study the ability of different groups to clear biofilm, wound tissues were collected after 3 days of different treatments, and the number of bacteria was determined by colony counting on agar plates (Figure S24). Compared with the control group, the survival rate of NPF@MN bacteria was significantly lower than that of the blank MN group and NPF group, which was due to the antimicrobial ability of NPF and the ability of MN to promote drug penetration at the wound site. Compared with the normal mice, diabetic mice with blank MNs (MN) interference exhibited slower healing speed, and *S. aureus* infection further deteriorated the wound healing and re-epithelialization of DUs (Fig. 6B-E). With treatment of MNs, promoted wound healing and neo-epithelialization were observed in *S. aureus*-infected

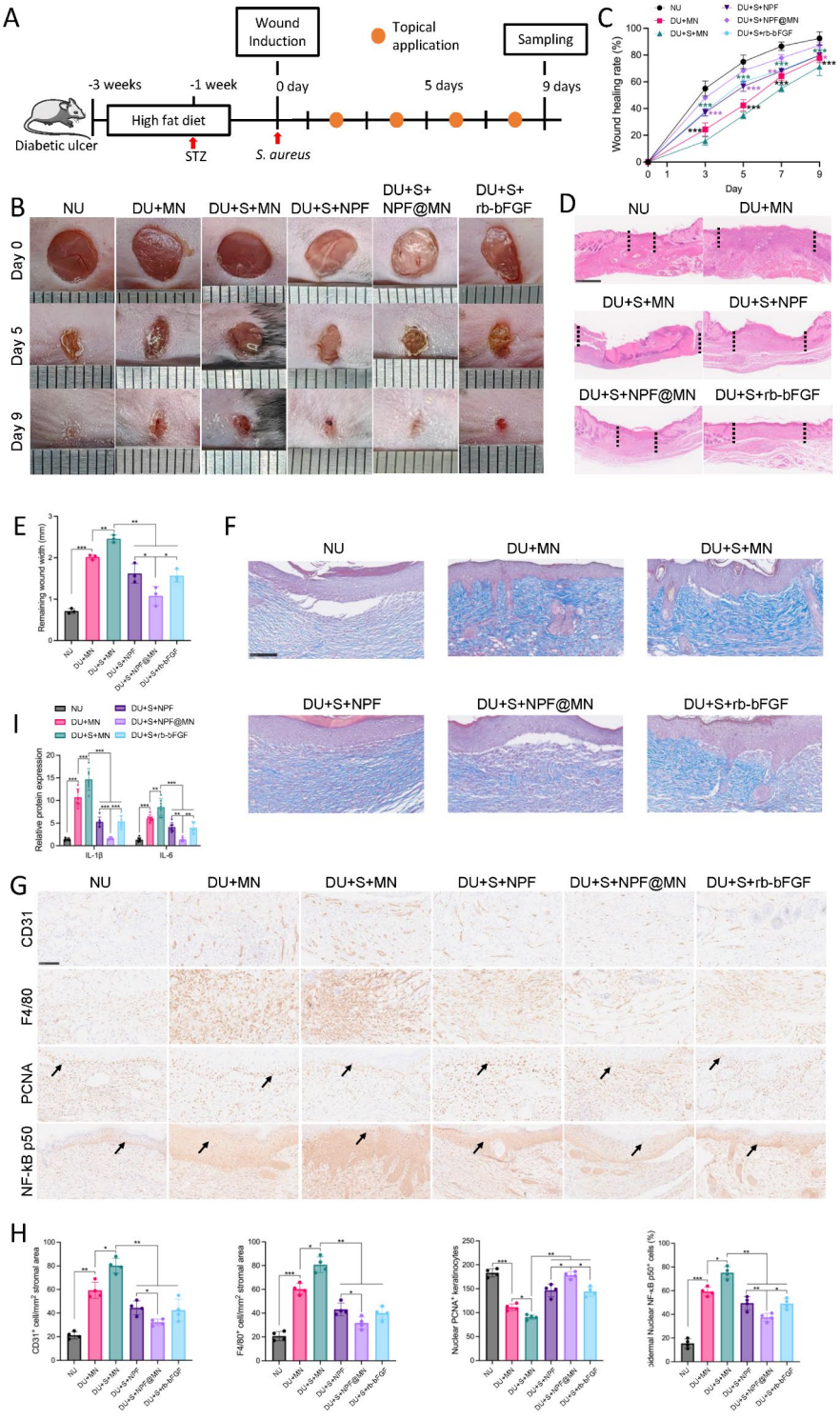

Fig. 6 NPF@MN effectively ameliorate the healing of *S. aureus*-infected DUs. (**A**) The workflow of animal experimental design. (**B**) The representative gross photograph of mice from NU group, DU + MN group, DU + *S. aureus* (S) + MN group, DU + *S. aureus* (S) + NPF group, DU + *S. aureus* (S) + NPF@MN group, and DU + *S. aureus* (S) + rb-bFGF group. (**C**) The quantification of healing process of different groups. $n = 4$ wounds/group. (**D**-**E**) The representative HE images of the skin wounds from day 9 and the relative quantification of remaining wound widths. Black dashed line indicated the boundary of epithelialization. Scale bar = 100 μm, $n = 3$ samples/group. (**F**) Masson's trichrome staining revealing the thickness of collagen fibers of different groups. Red indicates myofiber and blue represents collagenous fiber. Scale bar = 100 μm. (**G**-**H**) IHC staining of $CD31^+$, $F4/80^+$, $PCNA^+$, NF-kB $p50^+$ cells and the corresponding quantifications. Brown indicates positive. Black arrows: single nuclear positive. Scale bar = 100 μm, $n = 4$ samples/group. (**I**) The protein levels of *IL-1β* and *IL-6* detected by Bio-plex. $n = 7$ samples/group. $^{***}P < 0.001$, $^{**}P < 0.01$, $^{*}P < 0.05$

DUs, and notably, NPF@MN showed faster healing process, even than the positive group rb-bFGF (Fig. 6B-E). Masson's trichrome staining revealed that NPF@MN effectively reduced the excessive formation of collagen fibers in DUs infested with *S. aureus* at day 9 post-operationally, whose efficacy was more remarkable than both NPF and rb-bFGF (Fig. 6F). Immunohistochemical (IHC) staining of CD31, F4/80 and NF-kB p50 on day 9 after wounding indicated greater reduction of angiogenesis, macrophage infiltration and inflammation in infectious DUs by NPF@MN than NPF. NPF@MN significantly decreased the percentage of M1 macrophages ($iNOS^+$ stained) and stimulated the M2 polarization ($CD206^+$ labeled), with stronger effects compared with NPF and rb-bFGF (Figure S25). Consistent with the immunohistochemical results observed in mouse skin wounds, NPF@MN treatment exhibited the lowest CD80 (M1 marker) expression and the highest CD206 (M2 marker) expression (Figure S26). Moreover, proliferative keratinocytes ($PCNA^+$ marked) were elevated by NPF, NPF@MN and rb-bFGF, among which NPF@MN had the strongest effect (Fig. 6G, H). Bio-plex inflammatory factor detection showed that NPF, NPF@MN and rb-bFGF reduced the *IL-1β* and *IL-6* protein levels in DUs, and NPF@MN is the most effective strategy (Fig. 6I). H&E staining of liver, spleen and kidney from all groups showed no safety concern (Figure S27). Overall, NPF@MN effectively rescued the wound healing of DUs from *S. aureus* infection by expediting the re-epithelialization and M2 macrophage polarization, reducing inflammatory infiltration, angiogenesis and collagen deposit in the lateral healing process (day 9).

The transcriptional profiles of NPF@MN-treated S. aureus-infectious DUs

To study the altered genes after *S. aureus* execution, we investigated the DEGs ($|Log_2F\text{-}C| > 2$, and P-value < 0.05) between the DU+MN group and the DU+*S. aureus*+MN group into volcano plot using the high-throughput mRNA-seq, and 2,337 DEGs were identified after *S. aureus* induction (Fig. 7A). Among them, 1,454

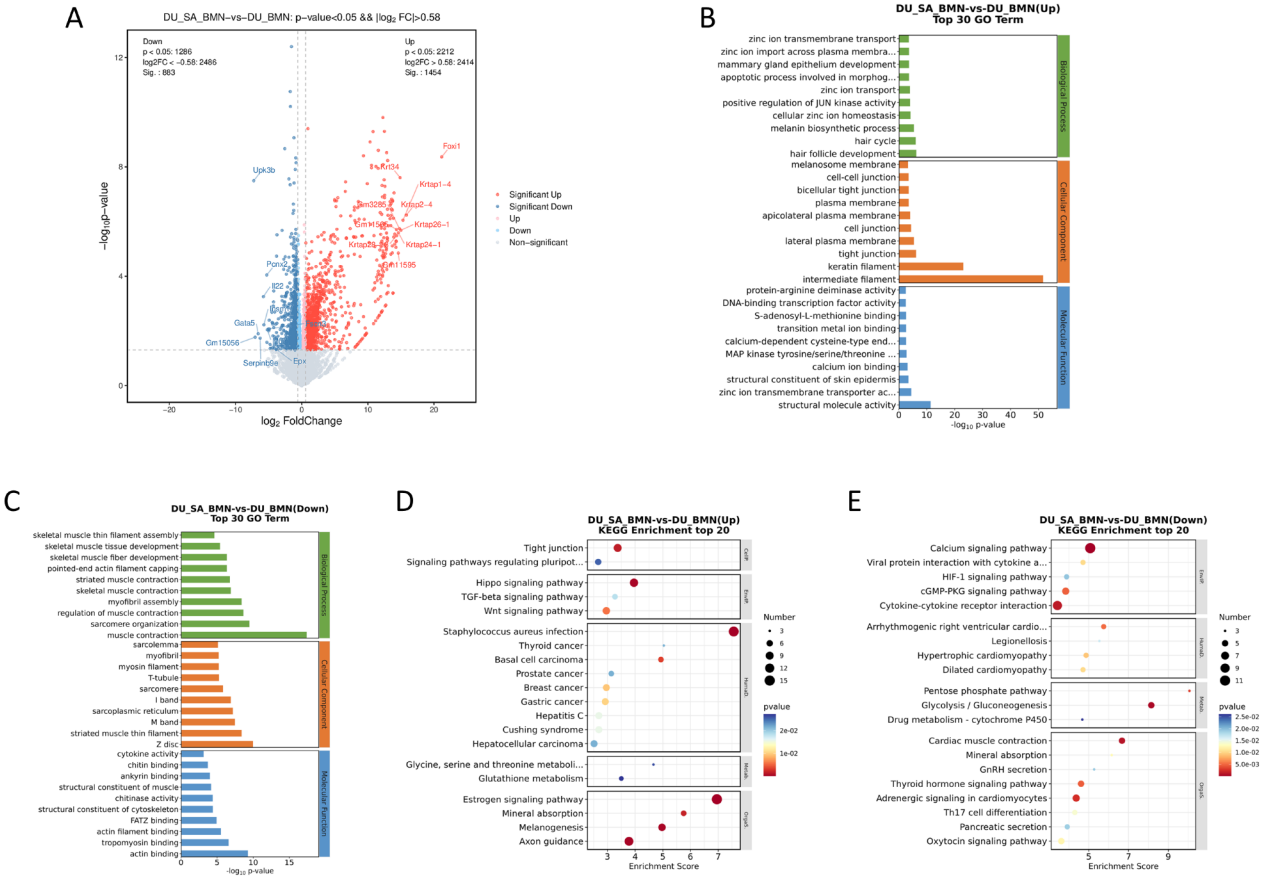

Fig. 7 The transcriptional profiles of *S. aureus*-infected DUs. (**A**) The volcano plot of the DEGs regulated by *S. aureus* (filtered by $|Log_2F\text{-}C| > 2$, and P-value < 0.05). (**B**, **C**) The top 30 up-regulated (**B**) and down-regulated (**C**) GO terms enriched by DEGs. (**D**, **E**) The top 20 up-regulated (**D**) and down-regulated (**E**) KEGG pathway enrichment of DEGs

(62.22%) genes were up-regulated, while 883 (37.78%) were markedly down-regulated.

To intuitively display the DEGs after *S. aureus* intervention, GO terms and KEGG pathway analysis were used to reveal the further association. GO analysis was performed by Fisher's exact test into three aspects (biological process, BP; cellular component, CC; molecular function, MF) with all the DEGs (Fig. 7B, C). The up-regulated GO category was mainly enriched in the celluar homeostasis and inflammation-related terms (such as hair follicle development, keratin filamentsuch and structural molecule activity) (Fig. 7B). In the down-regulated category, our analysis revealed that the the GO terms were mainly enriched in the muscular conditioning, indicating that *S. aureus* induction may participate in DUs inflammation and re-epithelialization processes (Fig. 7C). Moreover, KEGG pathway analysis (P-value$\leq$0.05) revealed that the up-regulated DEGs were enriched in metabolism-related pathways and inflammatory pathways (Fig. 7D). The pathways investigated include the estrogen signaling pathway, Wnt signaling pathway, and TGF-beta signaling pathway. The down-regulated DEGs were assigned into KEGG pathways and enrichment in signal transduction and inflammatory pathways were revealed, including calcium signaling pathway and cytokine-cytokine receptor interaction (Fig. 7E). Demonstrating that the *S. aureus* induction may take effects in DUs pathogenesis. The *S. aureus* induction may further deteriorate the morbid state of DUs by regulating these DEGs and pathways.

Additionally, we compared the DU+*S. aureus*+NPF@MN group with the paired control (DU+*S. aureus*+MN) group to investigate the therapeutic effects of NPF@MN in treating *S. aureus*-infected DUs. Among 1,467 changed genes, there were 527 (35.92%) up-regulated DEGs and 940 (64.08%) down-regulated DEGs after NPF@MN treatment (Fig. 8A), indicating the intrinsic alteration of DU conditions by NPF@-MNs.

To explore the therapeutic effects of NPF@MN treatment on DUs, we performed the depth association analysis. Bar charts were presented to show BP, CC, and MF aspects in GO analysis (Fig. 8B, C). The up-regulated category was mainly enriched in the skin barrier, intercellular structure and metabolism-related terms (such as establishment of skin barrier and keratinocyte proliferation) (Fig. 8B). In the down-related category, we found GO terms were mainly enriched in the biological status of cells, inflammatory-related terms, and metabolism-related signalings (Fig. 8C). These findings suggest that NPF@MN treatment may contribute to the pathogenesis and re-epithelialization processes in DUs. Moreover, the KEGG enrichment pathway analysis identified metabolism-related pathways as being influenced by NPF@MN treatment, mainly including steroid hormone biosynthesis, retinol metabolism and glucagon signaling pathway (Fig. 8D). Then, the down-regulated DEGs assigned to the KEGG pathways revealed enrichment in infection and metabolism-related pathways, mainly including estrogen signaling pathway, staphylococcus aureus infection, and GnRH secretion, demonstrating that the NPF@MN treatment may be effective in DUs treatment via those pathways (Fig. 8E).

To focus the function of NPF@MN on biofilm clearance, we utilized GSEA to analyze all the DEGs regulated by NPF@MN and the biofilm-related KEGG pathways were obtained. By comparing the altered pathways induced by NPF@MN in the transcriptional profiles with the GSEA results, we pinpointed the involvement of the insulin signaling pathway (Fig. 8F). IHC staining validated that NPF@MN upregulated the expression levels of Shc, IRS1 and IRS2 that were reduced in DUs with or without *S. aureus* infection (Fig. 8G, H). Quantitative analysis by western blotting (Figure S28) was further performed, which was consistent with the trend of immunohistochemistry results. NPF@MN might eliminate bacterial biofilm to relieve undue inflammation and ameliorate diabetic wound healing through the insulin signaling pathway.

Discussion

In this study, we fabricated a nanoformulation of MN, and loaded and delivered it into the wound epidermal of DUs with microneedles (NPF@MN), which exhibited excellent biocompatibility, drug-sustained release, pro-healing, antioxidant, and antibacterial properties without organ safe concern. The normal healing processes initiate from inflammation, then transit to re-epithelialization, and finally complete maturation phase and heal. Whereas, the inflammation of DUs is substandard and prolonged, hindering the epithelialization, collagen deposition and angiogenesis to occur in a timely, progressive fashion [53, 54]. With NPF@MN treatment, the healing speed of *S. aureus*-infected DUs was higher and the neo-epithelialization was more obvious than the positive drug rb-bFGF, showing remarkable efficacy in healing DUs. Decreased F4/80 and NF-kB p50 staining, reduced *IL-1β* and *IL-6* release, and increased $PCNA^+$ keratinocytes in the NPF@MN group demonstrated efficacious inflammation restriction and proliferation stimulation. M1 macrophages that participate in the inflammatory response to injuries and pathogens are dysregulated and the transition to M2 macrophages that exhibit anti-inflammation function are blocked in DUs [55]. The reduction of iNOS labeled M1 macrophages and the augment of M2 macrophages (CD206 stained) led by NPF@MN illustrated the pro-healing ability of NPF@MN through M2 macrophage polarization. Additionally, on day 9 after wounding, NPF@MN reduced the angiogenesis and deposition of collagen, which showed the closest morphology to the

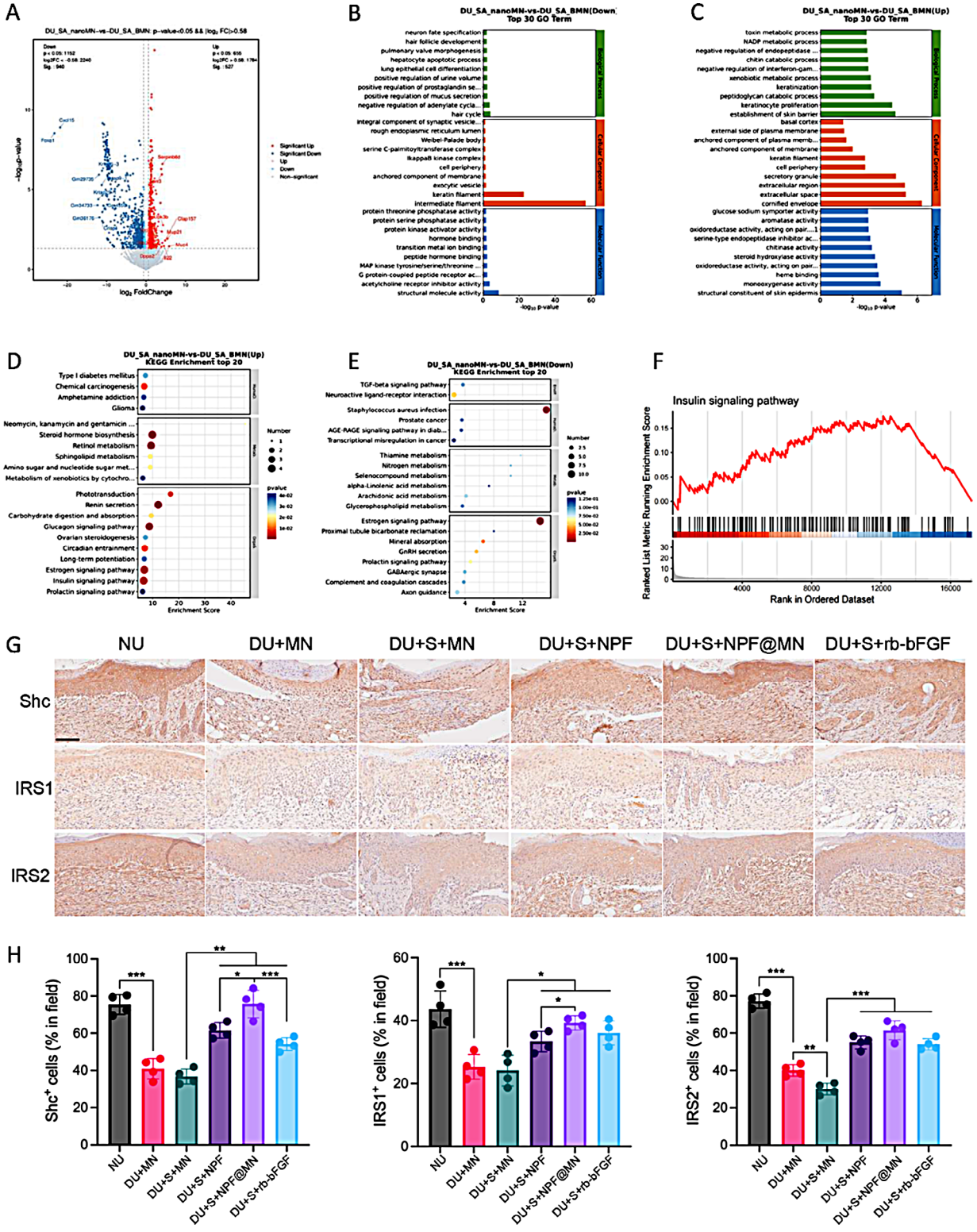

Fig. 8 The transcriptional profiles of NPF@MN-treated *S. aureus*-infectious DUs. (**A**) The volcano plot of the DEGs regulated by NPF@MN (filtered by $|Log_2F\text{-}C| > 2$, and *P*-value < 0.05). (**B**, **C**) The top 30 up-regulated (**B**) and down-regulated (**C**) GO terms enriched by DEGs. (**D**, **E**) The top 20 up-regulated (**D**) and down-regulated (**E**) KEGG pathway enrichment of DEGs. (**F**) The visualisation of insulin signaling pathway performed by R package "enrichplot". (**G**, **H**) The validation of the insulin signaling activation using IHC staining (**G**) and the relative quantification (**H**) in NU group, DU + MN group, DU + *S. aureus* (S) + MN group, DU + *S. aureus* (S) + NPF group, DU + *S. aureus* (S) + NPF@MN group, and DU + *S. aureus* (S) + rb-bFGF group. Brown indicates positive. $n = 4$ samples/group. $^{***}P < 0.001$, $^{**}P < 0.01$, $^{*}P < 0.05$

normal wound, implicating scar less healing. NPF@MN may be an ideal application to the breakthrough of biofilms and chronic inflammation in DU treatments.

To explore the mechanism of action of NPF@MN in conquering the biofilm and chronic healing of DUs, RNA-seq and GSEA analysis were performed and the insulin signaling pathway was identified as a key regulational path. The insulin signaling pathway is supposed to be activated during wound healing processes, while the expressions of the pathway-associated factors IR, IRS-1, IRS-2 and SHC are decreased in the DUs [56]. Systemic insulin treatment can improve the wound healing of DU patients [23]. Topical application of insulin improves the wound healing of diabetic mice, accelerates re-epithelialization and present anti-inflammation effects, shortening the inflammation phase to erect the subsequent processes [24, 25]. In human monocytic THP-1 cells, high glucose exposure results in elevated pro-inflammatory mediators and thereafter induced macrophage polarization toward M1 phenotype, which can be rescued by insulin stimulation [26]. The insulin signaling pathway is closely related to the healing of DUs and contributes to the downregulation of persistent chronic inflammation of DUs. NPF@MN may accelerate the diabetic healing and reduce the inflammatory infiltration by activating the insulin signaling pathway. Additionally, increasing evidence has reported that the insulin signaling pathway show a tight link to the biofilm formation [27–29]. Loss of function mutation in the gene that encodes the insulin-like receptor (*daf-2*) bacterial infection results in long-lived phenotype of *C. elegans* [57], and the bacterial biofilm established by *B. subtilis* downregulated the DAF-2 receptor [57]. Luteolin inhibits the growth of pathogenic bacteria via DAF-2/DAF-16 insulin-like signaling pathway [58]. Regarding the association between the insulin signaling pathway and the pathogen infection as well as bacterial biofilm formation, NPF@MN may eliminate the biofilm in the wound sites of DUs with the assistance of insulin signaling pathway. NPF@MN could be a desirable application to the management of intractable DUs perplexed by bacterial colonization and prolonged inflammation, which may be regulated by the insulin signaling pathway.

However, our study was only a proof of concept, and the Nisin used in the NPF@MN was mainly for the *S. aureus* wound infection model, and MNs were limited in their application to deeper tissue infections. In the next phase of our research, we will address the infection of severe wounds and modulate the microneedle release behavior for different infection models.

Conclusion

In conclusion, NPF-loaded multifunctional hyaluronic acid microneedles have been successfully prepared. The obtained NPF@MN show effective antibacterial and antibiofilm properties in vitro and in vivo. Meanwhile, NPF@MN had prominent antioxidant and anti-inflammatory properties which can scavenge ROS, thereby regulating macrophage polarization from the pro-inflammatory M1 phenotype to the M2 repair phenotype, promoting the formation of epithelial cells and the deposition of collagen simultaneously. Mechanistic studies have shown that NPF@MN can significantly improve diabetic wounds infected with Staphylococcus aureus biofilm by shortening the chronic inflammatory phase by regulating the insulin pathway. Compared with multicomponent therapy, NPF@MN component is simple and easy to prepare which have great clinical transformation potential for diabetic ulcer.

Materials and methods

Materials

DCFH-DA (The 3-hydroxytyramine hydrochloride and Diacetyldichlorofluorescein) probe were acquired from Sigma-Aldrich (St Louis, MO, USA). DMEM, penicillin-streptomycin (PS), and phosphate-buffered saline (PBS) were supplied by HyClone, headquartered in Logan, UT, USA. The following reagents and consumables are sourced from the same literature that we have previously published [59]: HaCaT was sourced from Cell Lines Service, Eppelheim, Germany, while high glucose DMEM medium was obtained from Gibco Co., Ltd. Sigma Co., Ltd provided MGO and bFGF, and Beyotime Co., Ltd supplied Cell Counting Kit-8 (CCK-8). C57BL/6J mice (male, 6–8 weeks, 20±5 g) were purchased from Shanghai SLAC Laboratory Animal Co., Ltd., Shanghai, China (SCXK (Hu) 2022–0004). High-fat and standard diets were procured from Shanghai Pu Lu Tong Biological Technology Co., Ltd. Sigma Co., Ltd provided Streptozotocin (STZ). Recombinant Bovine Basic Fibroblast Growth Factor (rb-bFGF, No. 20,160,102) was purchased from Zhuhai Yisheng Biopharmaceutical Co., Ltd. Antibodies used for immunohistochemistry (IHC) staining included anti-CD31 (diluted 1:2400, CST, #77,699), anti-F4/80 (diluted 1:600, CST, #70,076), anti-PCNA (diluted 1:1000, Abcam, ab29), anti-NF-kB p50 (diluted 1:36000, Abcam, ab32360), anti-iNOS (diluted 1:100, Abcam, ab283655), anti-CD206 (diluted 1:2000, Proteintech, 60143-1-Ig), anti-Shc (diluted 1:400, Abcam, ab33770), anti-IRS1 (diluted 1:50, Abcam, ab52167), and anti-IRS2 (diluted 1:200, Abcam, ab134101). Bio-Plex Pro Mouse Cytokine IL-1β (171G5002M) and Bio-Plex Pro Mouse Cytokine IL-6 kit (M600003G7V) were purchased from Bio-Rad Laboratories, Inc [59].

Bacterial culture and biofilm preparation

The standard strains of Gram-positive *Staphylococcus aureus* (ATCC 29,213) and Gram-negative *Escherichia coli* (ATCC 25,922) with good activity were selected for our experiments. The strains were inoculated on the solid agar medium for 12 h and then selected a single colony and cultured it in 25mL liquid LB medium at 37 ℃ for 18–24 h. The cultured strains were then harvested by centrifugation and washed with PBS for three times. The concentration of bacterial solution was measured by ultraviolet spectrophotometer at a wavelength of 600 nm. According to the colony counting method (CFU), re-adjust the OD 600 value of the bacterial stock solution to 0.1, which corresponds to 1×10^8 CFU/mL bacterial density.

400 μL of the bacterial suspension (1×10^8 CFU/mL) in the LB medium was added to the 24 well plate and cellulose film for the sake of bacterial biofilm. After that, the bacteria were cultured for 2 days, and the culture medium was changed once a day. The culture medium was discarded and washed the unattached bacteria with PBS for three times to harvest biofilms.

Preparation and characterization of Nisin-PA

The Nisin (10 mg, 1 mg/mL) was dissolved in 10 mL of ultrapure water under ultrasound (3 min). Afterward, PA (164.7μL, 2 mg/mL) was incrementally added to the solution under magnetic stirring, and the reaction proceeded in alkaline solution for 2 h. Then the product was dried in vacuo overnight to obtain Nisin-PA.

The products were characterized by UV–Vis absorption spectra, FTIR analysis, and 1 H NMR spectroscopy in D2O (Bruker AVANCE III HD 600 MHz) according to the previous literature [60].

Preparation of NPF

Different mass ratios of PA and Fe^{3+} (1:1, 2:1, 3:1) were used for constructing a pH-responsive nanocomplex via rapidly assembling of Schiff base and Fe-polyphenol complexation reaction. As an illustrative example, consider the synthesis steps in detail for a 3:1 ratio of PA to Fe^{3+}. Briefly, PA solution (164.7μL, 2 mg·mL^{-1}) was added dropwise to Nisin solution under magnetic stirring for 2 h at a speed of 500r. Afterward, $FeCl_3$ (71.4μL, 3 mg·mL^{-1}) was added and continued stirring for 30 min to obtain the pH-responsive NPF through Fe-polyphenol complexation interaction. The NPF dispersion was dialyzed in deionized water for 6 h (MWCO = 8000 Da) and subsequently dried under vacuum overnight to yield the NPF product.

Characterization of NPF

The particle size distribution, polydispersity index (PDI) and morphology of NPF were measured according to the previous literature methods [60]. The UV-Vis spectrometer was utilized to measure the UV-vis absorption of NPF and the OD value of free Nisin was measured at 270 nm to obtain standard curve. Moreover, the concentration of the NPF was defined by the Fe^{3+} content analyzed by ICP (ICP-OES, Agilent 720-ES).

Fabrication and characterization of MN

Hyaluronic acid powder (8000–10,000 Da) was dissolved in an NPF aqueous solution to obtain a 30% mass fraction HA solution. For HA MN preparation, the HA solution (w/t 30%) was poured onto PDMS molds under vacuum (~ 0.08 MPa), dried in a sealed desiccator overnight with the molds, peeled off, and stored in a sealed desiccator at room temperature. The dried NPF@MN were then examined for morphology using a microscope (Nikon ECLIPSE E 100, Nikon Corporation, Japan).

Insertion capability of the MN

The frozen section test assessed the insertion capability. MNs were applied to isolated rat skin for 15 min, followed by embedding the treated skin in OCT compound and freezing it at −80 °C. Subsequently, 10 μm sections were obtained from the frozen sample using a cryostat microtome (CRYOSTAR-NX50, Thermo, USA).

Hygroscopicity test

Store the dried MN in a sealed container under 75% humidity. Then MN was taken out and weighed every minute, a confocal microscope was used to take pictures of the microneedle changes in morphology.

In vitro stability and acid response-ability of NPF

The stability of NPF was detected according to the method in the references [60], and the acid responsiveness of NPF was detected by measuring the size of the sample and observing the morphological changes by TEM.

pH triggered Nisin release properties

To test and verify the pH sensitive character of NPF at different pH conditions, the release of Nisin from NPF was studied. Briefly, 0.2mL of NPF was well dispersed into 25 mL PBS with different pH (pH = 5.0, pH = 7.4 respectively). Then the suspensions were transferred into dialysis bags (MWCO 8KDa) and stirred at 37 °C with gentle agitation (100 rpm/min). Retrieve 2.0 mL of the sample solution at specified time intervals and replenish with an equivalent volume of PBS. The absorbance value of release free Nisin was measured by UV–vis spectrophotometer and analyzed according to the standard curve of the concentration of Nisin.

In vitro antioxidant tests

The antioxidant performance of samples with different PA-Fe mass ratios (1:1, 2:1, 3:1, 4:1) and different concentrations of NPF (31.25 μg/mL-1000 μg/mL) were evaluated by measuring the DPPH radical scavenging capacity. Briefly, 1mL of nanoparticle aqueous solution and DPPH ethanol solution (1mL 0.1mM) were thoroughly mixed and stirred at room temperature in the dark for 30 min, and then the wavelength of DPPH was scanned with an UV-Vis at a wavelength of 517 nm. The absorbance of the supernatant was read, measured three times parallel, and the inhibition ratio was calculated according to the following formula.

DPPH scavenging (%) = $(1\text{-}A_{sample}/A_{control}) \times 100\%$.

Where A are the absorbance value of the sample at 517 nm. The antioxidant performance of the sample under different pH was also tested.

Detection of reactive oxygen species

The scavenging capacity of NPF against intracellular ROS was detected by DCFH-DA probe, fluorescence imaging was performed by living cell workstation, flow cytometry was used for quantification. First, human fibroblast 3T3 cells were seeded in six-well plates (12×10^4 cells/mL) and incubated with NPF and NPF@MN for 6 h, the medium was then removed and treated with 0.3mM H_2O_2 for 30 min. Finally, the cells were incubated with DCFH-DA (10μM) in the dark at 37 ℃ for 20 min. Cell fluorescence intensity was imaged by living cell workstation and quantification of intracellular ROS level by flow cytometry analysis.

Scavenging of HO• and $O_2^{\bullet}$

In addition, we also selected two physiological related ROS, hydroxyl radical (• OH) and superoxide anion radical ($O_2^{\bullet-}$) to test the ROS scavenging capacity of NPF. First, we evaluated the scavenging efficiency of NPF for hydroxyl radicals by measuring the presence of fluorescent 2-hydroxyterephthalic acid. Briefly, a series of NPF (31.25 μg/mL-1000 μg/mL), TA (2mM), H_2O_2 (40 mM) were prepared in PBS (25 mM, pH=7.4) solution, and the mixture was incubated overnight on a shaker at 37℃ overnight. TA can react with hydrogen peroxide to generate 2-hydroxyterephthalic acid. The clearance rate of NPF to hydroxyl radicals was evaluated by measuring the fluorescence absorption value at 425 nm.

The scavenging capacity of NPF against superoxide anion was determined by the following methods. First, a series of NPF (62.5 to 1000 μg/mL) were prepared, and then were added to the solution containing 200μL Riboflavin (20 μM)、200μL methionine (12.5 mM) and 200 μL NBT(75 μM) and were incubated under ultraviolet radiation for 30 min, finally the absorbance of the mixture was measured. The positive control group was the sample containing riboflavin, methionine and NBT. All experiments were conducted in darkness.

Phenotype detection of RAW264.7 cells

After incubating RAW264.7 cells with DMEM and NPF@MN for 24 h, the treated cells were collected. Subsequently, they were sequentially stained with the CD80/CD206 antibody for 1 h, and the fluorescence signal of $CD80^+$/CD206 cells was measured using a flow cytometer.

Planktonic antibacterial studies

The antimicrobial properties of NPF@MN against *S. aureus* and *E. coli*. was determined through bacteriostatic zone test, time dependent germicidal test, concentration dependent germicidal test and live/dead test.

The MN and NPF@MN were dissolved in PBS solution, and the sterilized round filter paper with a diameter of 10 mm was soaked in it. The *S. aureus* and *E. coli* (diluted to 10^6 CFU/mL in LB medium) suspension (100 μL) were inoculated onto LB agar plates. The treated filter paper sheets were then placed on bacteria-coated agar plates, and the inhibition circle formed around the filter paper sheets were observed after incubation at 37 °C for 24 h.

For the time-dependent sterilization test, MN and NPF@MN were placed in 24-well plates with 1 mL of PBS at pH 5.5 and 7.4, respectively. 35μL of bacterial suspension is added, and after overnight incubation at 37 °C, serial dilutions are transferred to LB agar plates, and colonies are photographed and counted.

The antibacterial activity of various concentrations of NPF@MN was studied by standard plate count method, and the NPF@MN was dissolved in PBS solution and then was added to the 10^6 CFU/mL *E. coli* and *S. aureus* suspension. A 100 μL aliquot of the diluted bacterial solution was applied to agar plates, and colonies were observed.

Live/dead bacteria staining was used to study the viability of bacteria after exposure to MN, NPF and NPF@MN under different pH conditions. Qualitative assays were performed according to the manufacturer method. specifically, bacteria were mixed with dye solutions of SYTO 9 and propidium iodide for 0.5 h at room temperature, followed by imaging with Live-cell workstations. Living bacterial cells fluoresce green, and dead bacterial cells fluoresce red.

Biofilm antibacterial studies

The inhibition ability of NPF@MN on biofilm was determined by crystal violet staining, and the bacterial suspension was incubated in a 24-well plate for 2 days to obtain biofilm. The biofilm was incubated with MN, NPF and NPF@MN (concentration of 300 μg/mL) for 24 h, and then 500 μL of 0.1% v/v crystal violet ethanol solution

was added and soaked for 20 min. Bacterial growth was studied by measuring the absorbance of crystal violet solution at 590 nm by microplate reader.

The antibiofilm activity of NPF@MN was assessed by the number of CFUs. Inoculate 10 μL of diluted bacterial solutions (10^6 CFU/mL) at different pH values (pH = 7.4, pH = 5.5) into polycarbonate membrane placed on agar Petri dishes for 4 days to allow the formation of biofilm on the surface. After applying MN, NPF, and NPF@MN to the biofilm for 24 h, transfer the biofilm to a centrifuge tube containing 5 mL of liquid medium and vortex for 5 min. Colony counting was performed after overnight incubation by diluting the bacteria in PBS and inoculating them on LB agar plates. Additionally, the biofilm was stained using a bacterial live/dead kit.

Purchased 4–6 mm thick pig skin from a reagent distributor to create an ex vivo dermal wound model. Subsequently, the skin was cut into 5 cm * 5 cm squares. A spatula was used to create a scar on the skin that was 2 cm long and 1.5 mm deep to simulate an open wound. Next, immediately added 10 μL of bacterial suspension of 10^6 CFU/mL to each wound and then covered the inoculated wound with PBS-moistened gauze. The skins were treated with control, MN and NPF@MN groups and placed on solid agar plates and incubated in humidified atmosphere of 5% CO_2 at 37 °C for 24 h. After 24 h incubation, a 4.5 mm skin biopsy was collected from the center of the ex vivo wound model infection area. The extracted biopsy sample was placed in a 15 mL tube containing 5 mL PBS and ultrasonicated for 1 min. Ultimately, the bacterial solution was serially diluted and inoculated on LB agar plates to quantify the number of viable bacteria remaining in the wound.

In vitro DU model establishment

400 μM MGO was added to the culture medium of HaCaT cells for 48 h to construct inflammatory models of DUs. Different interposes were applied to observe the function of NPF@MN in regulating inflammatory cytokines.

Quantitative real-time PCR (qPCR)

Total mRNA was collected from the cell suspension or skin tissues of wounded mice on day 9 according to the manufacturer's instructions. The results were analyzed according to the previous literature methodology [59, 61]. The primers for qPCR are shown in Table S1.

Diabetic wound models and treatments

Eighteen Male C57BL/6J mice were kept in aseptic conditions at 23 ± 2 °C and randomly divided into 6 groups: normal ulcer (NU), DU applied with blank microneedles (DU + MN), DU infected with *S. aureus* and applied with MN (DU + *S. aureus* + MN), *S. aureus*-infected DU treated with NPF nanoparticles (DU + *S. aureus* + NPF), *S. aureus*-infected DU treated with NPF@MN (DU + *S. aureus* + NPF@ MN) and the positive group treated with rb-bFGF (DU + *S. aureus* + rb-bFGF) (n = 3 mice/group).

To establish STZ-induced diabetic models, fifteen C57BL/6J mice were placed on a high-fat diet for 2 weeks. Subsequently, they received intraperitoneal injections of STZ solution (0.2 mL in 0.1 M sodium citrate buffer) twice, with injections administered every other day. Mice that satisfied a blood glucose level > 16.7 mmol/L were considered qualified and used for wound punch (four 6-mm full-thickness excisional wounds). *S. aureus* was applied onto the wounds for 48 h(after punch to induce infection (10^7CFU and 20μL/wound), then different treatments (300 μg/mL/wound of NPF@MN; 30 ng/mouse of rb-bFGF) were conducted for 7 consecutive days and the wound skin tissues were collected on the day 9 for histological analysis and inflammatory factor detection. The mice were executed, and their livers, spleens and kidneys were taken for histopathological slide. All the above experimental procedures were permitted by the Ethics Committee of Yueyang Hospital of Integrated Traditional Chinese and Western Medicine, Shanghai University of TCM (YYLAC-2021-107-10, Supporting document 1).

Histology and immunohistochemical staining

The tissues were collected from mice and were stained with hematoxylin and eosin (H&E) and Masson's trichrome staining by the previous method to determine the remaining wound width and the degree of collagen fibers [59].

The tissue sections were deparaffinized, rehydrated, and subjected to IHC staining using the listed antibodies. The experimental results were analyzed according to previous literature reports [59, 61].

RNA isolation and library preparation

The extraction of total RNA from animal tissues and the method of library construction using the VAHTS Universal V6 RNA-seq Library Preparation Kit were based on previously published literature [59, 61].

RNA sequencing and differentially expressed genes analysis

Sequencing on an Illumina Novaseq 6000 platform produced paired-end reads with a length of 150 bp for the libraries. Raw reads for each sample were generated, then processed using fastp and the clean reads for subsequent analyses were obtained. Clean reads were mapped to the reference genome using HISAT2. The FPKM (Fragments Per Kilobase of exon model per Million mapped reads) for each gene was calculated, and HTSeq-count was utilized to obtain the read counts of each gene. R

software (v 3.2.0) was employed for PCA analysis to assess the biological duplication of samples. DESeq2 was applied for the differential expression analysis. Differentially expressed genes (DEGs) were selected based on P-value < 0.05 and $|\mathrm{Log_2foldchange}| > 2$. Hierarchical cluster analysis of DEGs was performed using R software to demonstrate the expression pattern of genes in different groups and samples.

Utilizing the hypergeometric distribution, we conducted Gene Ontology (GO) and Kyoto Encyclopedia of Genes and Genomes (KEGG) database enrichment analysis for the differentially expressed genes (DEGs) to identify significantly enriched terms. Terms and pathways with an adjusted P-value ≤ 0.05 in both GO and KEGG analyses were considered as significantly enriched.

GSEA analysis

GSEA (https://www.gsea-msigdb.org/gsea/index.jsp) was utilized to assess the functional enrichment and evaluate the DE mRNAs. Probes were ranked using signal-to-noise ratio, and statistical significance was determined through 1000 gene set permutations [58, 62]. Enrichment analysis was conducted using the R package "clusterProfiler," and the visualization of the insulin signaling pathway was carried out using the R package "enrichplot."

Statistical analysis

Data were presented as mean ± SD and analyzed using GraphPad Prism 8.0 software. Statistical analysis involved Student's t-test for comparing two groups and one-way ANOVA or 2-way ANOVA for multiple groups. A significance level of $P < 0.05$ was considered statistically significant. $^{***}P < 0.001$, $^{**}P < 0.01$, $^{*}P < 0.05$.

Supplementary Information

The online version contains supplementary material available at https://doi.org/10.1186/s12951-024-02731-x.

Figure S1. UV-Vis absorbance spectra of NPF nanoparticles at different proportions after incubation with DPPH. **Figure S2.** Clearance of DPPH by NPF with different proportions at pH7.4 and pH5.5. **Figure S3.** ^{1}H NMR spectrum of Nisin, PA and Nisin-PA in D_2O. **Figure S4.** UV-Vis absorbance spectra of NPF solution. **Figure S5.** Size stability of NPF in PBS and PBS containing 5%FBS for 48 h. **Figure S6.** NPF nanoparticle composition content. **Figure S7.** Zeta potential of NPF at different pH conditions. **Figure S8.** Calibration curve of Nisin. **Figure S9.** Microneedle OCT optical coherence test. **Figure S10.** Representative image of the distribution of RhB@MN and RhB on the skin surface. **Figure S11.** Force-displacement curves of microneedle NPF@MN. **Figure S12.** OCT images of microlesions and microchannels produced by microneedles piercing the skin. **Figure S13.** UV-Vis absorption spectra recorded after different concentration of NPF. **Figure S14.** Quantitative of NPF scavenging capacity for hydroxyl radicals. **Figure S15.** Quantitative plots of the superoxide anion scavenging capacity of NPF and vitamin C at different concentrations. **Figure S16.** Hemolytic properties of NPF. **Figure S17.** Cell viability of human dermal fibroblasts treated with Nisin, NPF and NPF@MN (50–1000 μg/mL) for 24 h and then incubated with 3 mM H_2O_2 for 30 min. 293T cells incubated in normal cell culture medium were applied as the control group. $n = 3$ samples/group. **Figure S18.** The fluorescent photograph of 293T cells co-cultured with Nisin, NPF and NPF@MN for 24 h. Bar = 1000 μm. $n = 3$ samples/group. **Figure S19.** Quantification of the $CD206^+$of RAW264.7 cells intensity. **Figure S20.** Western blot analysis to determine the protein levels of CD80 and CD206 in macrophages. **Figure S21.** A-B The level of *IL-1β* and *IL-10* inflammatory factor. **Figure S22.** Relative fluorescence intensities of different groups (Control, MN, NPF and NPF@MN) of stained immunofluorescence images of E. coli (A) and Staphylococcus aureus (B) **Figure S23.** The healing rate of wounds treated with different concentration of NPF@MN. **Figure S24.** (A) Representative photographs of bacterial cultures from skin tissue from wounds of diabetic mice infected with biofilm and (B) sterilization results on Day 3, characterized by a standard plate counting assay. **Figure S25**. A-B. IHC staining of $iNOS^+$ and $CD206^+$ cells and the corresponding quantifications. **Figure S26.** (**A**) Representative flow cytometry plots of $CD206^+$ and $CD80^+$. Quantitative analysis of (**B**) $CD206^+$ ($n = 3$) and (**C**) $CD80^+$ ($n = 3$) fluorescence intensity. **Figure S27**. The H&E staining of liver, kidney and spleen from different groups. **Figure S28.** (A-D) IRS1, IRS2 and Shc protein levels detected by western blotting (ns represented not significant. **Table S1.** Primers for qPCR.

Acknowledgements

National Natural Science Foundation of China (No. 82374444), Xinglin Youth Scholar of Shanghai University of Traditional Chinese Medicine (No. RY411.33.10), Youth Talent Promotion Project of China Association of Traditional Chinese Medicine (2021–2023) Category A (No. CACM-2021-QNRC2-A10), Health Young Talents of Shanghai Municipal Health Commission (No. 2022YQ026), "Chen Guang" project supported by Shanghai Municipal Education Commission and Shanghai Education Development Foundation (No. 22CGA50), Shanghai Science and Technology Development Funds (Sailing Program) (No. 23YF1439800). Talent Program of Shanghai Municipal Health Commission (No. 2022XD052), Sci-Tech Innovation 2030-Major Project of Brain science and brain-inspired intelligence technology (No. 2021ZD0202003), Shanghai Dermatology Research Center (No. 2023ZZ02017), and Shanghai Skin Disease Hospital demonstration research ward project (No. SHDC2023CRW009).

Author contributions

The following is an "author contribution list" that includes the name of each author and their contribution to the work.Y.L. and Y.Y. designed the research. Y.Y., L.F., and J.J. performed experiments and analyzed data. J.S., L.X.,X.M. and L.K. provided resources or conducted experiments. Y.Y., L.F., and J.J. wrote the manuscript and prepared all fgures. B.L. and Y. L.: Writing-Reviewing and Editing, Funding acquisition. All authors reviewed the manuscript.

Data availability

No datasets were generated or analysed during the current study.

Declarations

Competing interests

The authors declare no competing interests.

Author details

[1]The Institute for Biomedical Engineering & Nano Science, School of Medicine, Shanghai Skin Disease Hospital of Tongji University, Tongji University, Shanghai 200092, China
[2]Shanghai Skin Disease Hospital, Institute of Dermatology, School of Medicine, Tongji University, Shanghai 200443, China
[3]Department of Dermatology, Yueyang Hospital of Integrated Traditional Chinese and Western Medicine, Shanghai University of Traditional Chinese Medicine, Shanghai 200437, China
[4]Institute of Dermatology, Shanghai Academy of Traditional Chinese Medicine, Shanghai 201203, China

Received: 6 May 2024 / Accepted: 22 July 2024
Published online: 14 August 2024

References

1. Lim JZM, Ng NSL, Thomas C. Prevention and treatment of diabetic foot ulcers. J R Soc Med. 2017;110(3):104–9.

2. Holl J, Kowalewski C, Zimek Z, Fiedor P, Kaminski A, Oldak T, Moniuszko M, Eljaszewicz A. Chronic Diabetic wounds and their treatment with skin substitutes. Cells. 2021;10(3):21.
3. Jiang X, Ma J, Xue K, Chen J, Zhang Y, Zhang G, Wang K, Yao Z, Hu Q, Lin C, Lei B, Mao C. Highly bioactive MXene-M2-Exosome nanocomposites promote angiogenic Diabetic Wound Repair through reconstructing high glucose-derived Immune Inhibition. ACS Nano. 2024;18(5):4269–86.
4. Cai Y, Chen K, Liu C, Qu X. Harnessing strategies for enhancing diabetic wound healing from the perspective of spatial inflammation patterns. Bioactive Mater. 2023;28:243–54.
5. Landén NX, Li D, Ståhle M. Transition from inflammation to proliferation: a critical step during wound healing. Cell Mol Life Sci. 2016;73(20):3861–85.
6. Shi Y, Wang S, Wang K, Yang R, Liu D, Liao H, Qi Y, Qiu K, Hu Y, Wen H, Xu K. Relieving Macrophage Dysfunction by Inhibiting SREBP2 Activity: A Hypoxic Mesenchymal Stem Cells-Derived Exosomes Loaded Multifunctional Hydrogel for Accelerated Diabetic Wound Healing, Small n/a(n/a) (2024) 2309276.
7. Louiselle AE, Niemiec SM, Zgheib C, Liechty KW. Macrophage polarization and diabetic wound healing. Translational Res. 2021;236:109–16.
8. Sun C, Zhou X, Liu C, Deng S, Song Y, Yang J, Dai J, Ju Y. An Integrated Therapeutic and Preventive Nanozyme-based Microneedle for Biofilm-Infected Diabetic Wound Healing. Adv Healthc Mater. 2023;12(30):2301474.
9. Rehak L, Giurato L, Meloni M, Panunzi A, Manti GM, Uccioli L. The Immune-Centric Revolution in the Diabetic Foot: Monocytes and Lymphocytes Role in Wound Healing and tissue Regeneration—A narrative review. J Clin Med, 2022.
10. Shinjo T, Li Q, Ishikado A, Park K, St-Louis R, Yokomizo H, Fu J, Yu M.G., Wang H., Hasturk H., Van Dyke T.E., King G.L. Insulin's regulation of CXCL1 expression is critical for Neutrophil recruitments and the development of Periodontitis and Poor Wound Healing in Diabetes. Diabetes. 2019;68(Supplement1):628–P.
11. Lee C-H, Hung K-C, Hsieh M-J, Chang S-H, Juang J-H, Hsieh IC, Wen M-S, Liu S-J. Core-shell insulin-loaded nanofibrous scaffolds for repairing diabetic wounds. Nanomed Nanotechnol Biol Med. 2020;24:102123.
12. Peterson C, Chandler HL. Insulin facilitates corneal wound healing in the diabetic environment through the RTK-PI3K/Akt/mTOR axis in vitro. Mol Cell Endocrinol. 2022;548:111611.
13. Wertheimer E, Spravchikov N, Trebicz M, Gartsbein M, Accili D, Avinoah I, Nofeh-Moses S, Sizyakov G, Tennenbaum T. The regulation of skin proliferation and differentiation in the IR null mouse: implications for skin complications of diabetes. Endocrinology. 2001;142(3):1234–41.
14. Yu T, Gao M, Yang P, Pei Q, Liu D, Wang D, Zhang X, Liu Y. Topical insulin accelerates cutaneous wound healing in insulin-resistant diabetic rats. Am J Transl Res. 2017;9(10):4682–93.
15. Lu Y, Zhao M, Peng Y, He S, Zhu X, Hu C, Xia G, Zuo T, Zhang X, Yun Y, Zhang W, Shen X. A physicochemical double-cross-linked gelatin hydrogel with enhanced antibacterial and anti-inflammatory capabilities for improving wound healing. J Nanobiotechnol. 2022;20(1):426.
16. Yu T, Gao M, Yang P, Liu D, Wang D, Song F, Zhang X, Liu Y. Insulin promotes macrophage phenotype transition through PI3K/Akt and PPAR-γ signaling during diabetic wound healing. J Cell Physiol. 2019;234(4):4217–31.
17. Hall JA, Ramachandran D, Roh HC, DiSpirito JR, Belchior T, Zushin P-JH, Palmer C, Hong S, Mina AI, Liu B, Deng Z, Aryal P, Jacobs C, Tenen D, Brown CW, Charles JF, Shulman GI, Kahn BB, Tsai LTY, Rosen ED, Spiegelman BM, Banks AS. Obesity-linked PPARγ S273 phosphorylation promotes insulin resistance through growth differentiation factor 3. Cell Metabol. 2020;32(4):665–e6756.
18. Papuc C, Goran GV, Predescu CN, Tudoreanu L, Ştefan G. Plant polyphenols mechanisms of action on insulin resistance and against the loss of pancreatic beta cells. Crit Rev Food Sci Nutr. 2021;62(2):325–52.
19. Yan L, Guo X, Zhou J, Zhu Y, Zhang Z, Chen H. Quercetin prevents intestinal stem cell aging via scavenging ROS and inhibiting insulin signaling in Drosophila. Antioxidants. 2023;12(1):59.
20. Knezevic S, Ghafoor A, Mehri S, Barazi A, Dziura M, Trant JF, Dieni CA. Catechin and other catechol-containing secondary metabolites: bacterial biotransformation and regulation of carbohydrate metabolism. PharmaNutrition. 2021;17:100273.
21. Shahwan M, Alhumaydhi F, Ashraf GM, Hasan PMZ, Shamsi A. Role of polyphenols in combating type 2 diabetes and insulin resistance. Int J Biol Macromol. 2022;206:567–79.
22. Wu X, Liu L, Zheng Q, Hao H, Ye H, Li P, Yang H. Protocatechuic aldehyde protects cardiomycoytes against ischemic injury via regulation of nuclear pyruvate kinase M2. Acta Pharm Sinica B. 2021;11(11):3553–66.
23. Fu Y-J, Shi Y-F, Wang L-Y, Zhao Y-F, Wang R-K, Li K, Zhang S-T, Zha X-J, Wang W, Zhao X, Yang W. All-natural immunomodulatory Bioadhesive Hydrogel promotes Angiogenesis and Diabetic Wound Healing by regulating macrophage heterogeneity. Adv Sci. 2023;10(13):2206771.
24. Cao M, Wang J, Jiang X, Sun Z, Zhao L, Chen G. Phenolic constituents from Black Quinoa Alleviate Insulin Resistance in HepG2 cells via regulating IRS1/PI3K/Akt/GLUTs signaling pathways. J Agric Food Chem. 2023;71(48):18780–91.
25. Xiong R, Wang X-L, Wu J-M, Tang Y, Qiu W-Q, Shen X, Teng J-F, Pan R, Zhao Y, Yu L, Liu J, Chen H-X, Qin D-L, Yu C-L, Wu A-G. Polyphenols isolated from lychee seed inhibit Alzheimer's disease-associated tau through improving insulin resistance via the IRS-1/PI3K/Akt/GSK-3β pathway. J Ethnopharmacol. 2020;251:112548.
26. Miao L, Zhang X, Zhang H, Cheong MS, Chen X, Farag MA, Cheang WS, Xiao J. Baicalin ameliorates insulin resistance and regulates hepatic glucose metabolism via activating insulin signaling pathway in obese pre-diabetic mice. Phytomedicine. 2024;124:155296.
27. Durand B, Pouget C, Magnan C, Molle V, Lavigne JP. C. Dunyach-Remy, bacterial interactions in the Context of Chronic Wound Biofilm: a review. Microorganisms 10(8) (2022).
28. de Vor L, Rooijakkers SHM, van Strijp JAG. Staphylococci evade the innate immune response by disarming neutrophils and forming biofilms. FEBS Lett. 2020;594(16):2556–69.
29. Cho H, Blatchley MR, Duh EJ, Gerecht S. Acellular and cellular approaches to improve diabetic wound healing. Adv Drug Deliv Rev. 2019;146:267–88.
30. Yang L, Zhang D, Li W, Lin H, Ding C, Liu Q, Wang L, Li Z, Mei L, Chen H, Zhao Y, Zeng X. Biofilm microenvironment triggered self-enhancing photodynamic immunomodulatory microneedle for diabetic wound therapy. Nat Commun. 2023;14(1):7658.
31. Mondal A, Singha P, Douglass M, Estes L, Garren M, Griffin L, Kumar A, Handa H. A synergistic New Approach toward enhanced Antibacterial Efficacy via Antimicrobial peptide immobilization on a nitric oxide-releasing surface. ACS Appl Mater Interfaces. 2021;13(37):43892–903.
32. Fan D, Liu X, Ren Y, Luo Z, Li Y, Dong J, Wegner SV, Chen F, Zeng W. Harnessing antimicrobial peptide-coupled photosensitizer to combat drug-resistant biofilm infections through enhanced photodynamic therapy. Acta Pharm Sinica B. 2024;14(4):1759–71.
33. Su Y, Andrabi SM, Shahriar SMS, Wong SL, Wang G, Xie J. Triggered release of antimicrobial peptide from microneedle patches for treatment of wound biofilms. J Controlled Release. 2023;356:131–41.
34. Ashrafi M, Novak-Frazer L, Morris J, Baguneid M, Rautemaa-Richardson R, Bayat A. Electrical stimulation disrupts biofilms in a human wound model and reveals the potential for monitoring treatment response with volatile biomarkers. Wound Repair Regen. 2019;27(1):5–18.
35. Jamaledin R, Yiu CKY, Zare EN, Niu LN, Vecchione R, Chen GJ, Gu Z, Tay FR. Makvandi, advances in Antimicrobial Microneedle patches for combating infections. Adv Mater. 2020;32(33):29.
36. Xu JH, Danehy R, Cai HW, Ao Z, Pu M, Nusawardhana A, Rowe-Magnus D, Guo F. Microneedle Patch-mediated treatment of bacterial biofilms. ACS Appl Mater Interfaces. 2019;11(16):14640–6.
37. Wang X, Qian J-q, Yin J-l, Gong F, Guo H. Preparation and antibacterial properties of high-methoxy pectin oligosaccharide -nisin nanoparticles. Eur Polymer J. 2023;200:112472.
38. Gan D, Xing W, Jiang L, Fang J, Zhao C, Ren F, Fang L, Wang K, Lu X. Plant-inspired adhesive and tough hydrogel based on Ag-Lignin nanoparticles-triggered dynamic redox catechol chemistry. Nat Commun 10(1) (2019).
39. Zheng D-W, Lei Q, Zhu J-Y, Fan J-X, Li C-X, Li C, Xu Z, Cheng S-X, Zhang X-Z. Switching apoptosis to ferroptosis: metal–Organic Network for High-Efficiency Anticancer Therapy. Nano Lett. 2016;17(1):284–91.
40. Liu CY, Shen WW, Li BN, Li TF, Chang H, Cheng YY. Natural polyphenols augment cytosolic protein delivery by a functional polymer. Chem Mat. 2019;31(6):1956–65.
41. Liang YQ, Li ZL, Huang Y, Yu R, Guo BL. Dual-Dynamic-Bond cross-linked Antibacterial Adhesive Hydrogel sealants with On-Demand removability for Post-wound-closure and Infected Wound Healing. ACS Nano. 2021;15(4):7078–93.
42. Li MY, Wang H, Hu JF, Hu JJ, Zhang S, Yang Z, Li YW, Cheng YY. Smart Hydrogels with Antibacterial properties built from all Natural Building blocks. Chem Mat. 2019;31(18):7678–85.
43. Filippidi E, Cristiani TR, Eisenbach CD, Waite JH, Israelachvili JN, Ahn BK, Valentine MT. Toughening elastomers using mussel-inspired iron-catechol complexes. Science. 2017;358(6362):502–5.
44. Fullenkamp DE, Barrett DG, Miller DR, Kurutz JW, Messersmith PB. pH-dependent cross-linking of catechols through oxidation via Fe3 + and potential implications for mussel adhesion. RSC Adv. 2014;4(48):25127–34.

45. Badhani B, Sharma N, Kakkar R. Gallic acid: a versatile antioxidant with promising therapeutic and industrial applications. RSC Adv. 2015;5(35):27540–57.
46. Lu YP, Zhao MH, Peng Y, He SZ, Zhu XP, Hu C, Xia GH, Zuo T, Zhang XY, Yun YH, Zhang WM, Shen XR. A physicochemical double-cross-linked gelatin hydrogel with enhanced antibacterial and anti-inflammatory capabilities for improving wound healing. J Nanobiotechnol. 2022;20(1):26.
47. Charkoudian LK, Franz KJ. Fe(III)-coordination properties of neuromelanin components: 5,6-dihydroxyindole and 5,6-dihydroxyindole-2-carboxylic acid. Inorg Chem. 2006;45(9):3657–64.
48. Liu J, Liu Y. Research advances on the formation mechanism and diagnosis of bacteria biofilms in chronic wounds, Zhonghua shao shang za zhi = Zhonghua Shaoshang zazhi = Chinese. J Burns. 2021;37(7):692–6.
49. Blicharz TM, Gong P, Bunner BM, Chu LL, Leonard KM, Wakefield JA, Williams RE, Dadgar M, Tagliabue CA, El Khaja R, Marlin SL, Haghgooie R, Davis SP, Chickering DE, Bernstein H. Microneedle-based device for the one-step painless collection of capillary blood samples. Nat Biomed Eng. 2018;2(3):151–7.
50. Qi X, Cai E, Xiang Y, Zhang C, Ge X, Wang J, Lan Y, Xu H, Hu R, Shen J. An Immunomodulatory Hydrogel by Hyperthermia-assisted Self-Cascade glucose depletion and ROS scavenging for Diabetic Foot Ulcer Wound therapeutics. Adv Mater. 2023;35(48):2306632.
51. Ch'ng JH, Chong KKL, Lam LN, Wong JJ, Kline KA. Biofilm-associated infection by enterococci. Nat Rev Microbiol. 2019;17(2):82–94.
52. Nath M, Song XQ, Eng G, Kumar A. Synthesis and spectral studies of organotin(IV) 4-amino-3-alkyl-1,2,4-triazole-5-thionates: in vitro antimicrobial activity, Spectroc. Acta Pt. A-Molec. Biomolec Spectr. 2008;70(4):766–74.
53. Wu Y, Quan Y, Liu Y, Liu K, Li H, Jiang Z, Zhang T, Lei H, Radek K, Li D, Wang Z, Lu J, Wang W, Ji S, Xia Z, Lai Y. Hyperglycaemia inhibits REG3A expression to exacerbate TLR3-mediated skin inflammation in diabetes. Nat Commun. 2016;7:13393.
54. Rai V, Moellmer R, Agrawal DK. The role of CXCL8 in chronic nonhealing diabetic foot ulcers and phenotypic changes in fibroblasts: a molecular perspective. Mol Biol Rep. 2022;49(2):1565–72.
55. Boniakowski AE, Kimball AS, Jacobs BN, Kunkel SL, Gallagher KA. Macrophage-mediated inflammation in Normal and Diabetic Wound Healing. J Immunol. 2017;199(1):17–24.
56. Lima MHM, Caricilli AM, de Abreu LL, Araujo EP, Pelegrinelli FF, Thirone ACP, Tsukumo DM, Pessoa AFM, dos Santos MF, de Moraes MA, Carvalheira JBC, Velloso LA, Saad MJA. Topical insulin accelerates Wound Healing in Diabetes by enhancing the AKT and ERK pathways: a double-blind placebo-controlled clinical trial. PLoS ONE. 2012;7(5):13.
57. Garsin DA, Villanueva JM, Begun J, Kim DH, Sifri CD, Calderwood SB, Ruvkun G, Ausubel FM. Long-lived C-elegans daf-2 mutants are resistant to bacterial pathogens. Science. 2003;300(5627):1921–1921.
58. Reimand J, Isserlin R, Voisin V, Kucera M, Tannus-Lopes C, Rostamianfar A, Wadi L, Meyer M, Wong J, Xu CJ, Merico D, Bader GD. Pathway enrichment analysis and visualization of omics data using g:Profiler, GSEA, Cytoscape and EnrichmentMap. Nat Protoc. 2019;14(2):482–517.
59. Yang Y, Yang Y, Jiang J, Wu Z, Sun J, Zhi H, Chen S, Kuai L, Li B, Dong H. Arginine-nanoenzyme with timely angiogenesis for promoting Diabetic Wound Healing. ACS Appl Mater Interfaces. 2024;16(8):9640–55.
60. Zang J, Yang Y, Zheng X, Yang Y, Zhao Y, Miao Z, Zhang T, Gu J, Liu Y, Yin W, Ma X, Ding Q, Dong H, Li Y, Li Y. Dynamic tagging to drive arginine nanoassembly to metabolically potentiate immune checkpoint blockade therapy. Biomaterials. 2023;292:121938.
61. Jiang J-S, Zang J, Ru Y, Luo Y, Song J-K, Luo Y, Fei X-Y, Zhang Z, Zhang Y, Yang D, Zhou M, Chen Q-L, Bai Y, Li Y-Y, Kuai L, Li B. Patient-driven discovery of CCN1 to rescue cutaneous wound healing in diabetes via the intracellular EIF3A/CCN1/ATG7 signaling by nanoparticle-enabled delivery. Biomaterials. 2022;288:121698.
62. Subramanian A, Tamayo P, Mootha VK, Mukherjee S, Ebert BL, Gillette MA, Paulovich A, Pomeroy SL, Golub TR, Lander ES, Mesirov JP. Gene set enrichment analysis: a knowledge-based approach for interpreting genome-wide expression profiles. Proc Natl Acad Sci U S A. 2005;102(43):15545–50.

Publisher's Note